pH-Sensitive Hybrid System Based on Eu3+/Gd3+ Co-doped Hydroxyapatite and Mesoporous Silica Designed for Theranostic Applications

Rafaela Caroline Rodrigues Apostolos , Andreza Sousa Andrada , André Felipe de Oliveira , Ernesto Soares de Freitas Neto , Edesia Martins Barros de Sousa *

Posted Date: 19 May 2023

doi: 10.20944/preprints202305.1385.v1

Keywords: smart drug delivery system; nanomaterials; poly(methacrylic acid); photoluminescence

Article

pH-Sensitive Hybrid System Based on Eu^{3+}/Gd^{3+} Co-doped Hydroxyapatite and Mesoporous Silica Designed for Theranostic Applications

Rafaela Caroline Rodrigues Apostolos [1], Andreza Sousa Andrada [2], André Felipe de Oliveira [1], Ernesto Soares de Freitas Neto [2] and Edésia Martins Barros de Sousa [1,*]

[1] Centro de Desenvolvimento da Tecnologia Nuclear – CDTN – Avenida Presidente Antônio Carlos, 6.627 - Campus UFMG, CEP 31270-901, Belo Horizonte, Minas Gerais, Brazil
[2] Universidade Federal de Itajubá – UNIFEI - Rua São Paulo 377 Campus Itabira, CEP 35903-087, Minas Gerais, Brazil
* Correspondence: sousaem@cdtn.br

Abstract: Nanomaterials such as pH-responsive polymers are promising for targeted drug delivery systems, due to the difference in pH between tumor and healthy regions. However, there is a significant concern about the application of these materials in this field due to their low mechanical resistance, which can be mitigated by combining these polymers with mechanically resistant inorganic materials such as mesoporous silica nanoparticles (MSN) and hydroxyapatite (HA). Mesoporous silica has interesting properties such as high surface area and hydroxyapatite has been widely studied to aid in bone regeneration, providing special properties adding multifunctionality to the system. Furthermore, fields of medicine involving luminescent elements such as rare earth are an interesting option in cancer treatment. The present work aims to obtain a pH-sensitive hybrid system based on silica and hydroxyapatite with photoluminescent and magnetic properties. The nanocomposites were characterized by X-ray diffraction (XRD), Fourier transform infrared spectroscopy (FTIR), nitrogen adsorption methods, CHN elemental analysis, Zeta Potential, scanning electron microscopy (SEM), and transmission electron microscopy (TEM), vibrational sample magnetometry (VSM), and photoluminescence analysis. Incorporation and release studies of the antitumor drug doxorubicin were performed to evaluate the potential use of these systems in targeted drug delivery. The results showed the luminescent and magnetic properties of the materials and showed suitable characteristics for application in the release of pH-sensitive drugs.

Keywords: smart drug delivery system; nanomaterials; poly(methacrylic acid); photoluminescence

1. Introduction

Cancer is the leading cause of death in both developed and developing countries. Although medical advances have improved patient survival, the side effects caused by chemotherapy treatments, such as pain, fatigue, nausea, and vomiting, can negatively affect people's quality of life [1]. Doxorubicin (DOX) is a well-known example of a drug used in the treatment of this pathology [2] and some studies show several limitations of this drug that include uncontrolled release rate, cardiotoxicity, toxicity to normal cells, among others. The toxicity of normal cells, caused by the lack of distinction between normal and tumor cells, demonstrates the emerging need to develop targeted delivery systems for the tumor region [3].

The tumor microenvironment has several characteristics that distinguish it from normal tissue. Studies show that tumor cells produce higher levels of lactic acid, which can lead to a more acidic environment, a phenomenon known as "tumor acidosis" [4]. Therefore, the pH of tumor tissues presents values that can vary from 6.5-7.2, or even reach a lower value, while the pH of healthy tissues presents a slightly alkaline range of 7.35-7.45. Despite this, it is important to highlight that the pH of

 doi:10.20944/preprints202305.1385.v1

tumor tissues can vary depending on several factors, including the type and stage of cancer, the location of the tumor, and the metabolic activity of tumor cells [5].

The existing pH difference between healthy and tumor cells has encouraged the scientific community to develop drug delivery systems that are stable at physiological pH and selectively release the antitumor drug into the cancerous region. Studies of versatile drug nanocarriers, including liposomes, dendrimers, polymeric nanoparticles, and inorganic nanoparticles have shown potential, in this type of application [6].

Among these, pH-responsive polymeric nanomaterials have been explored in some studies of targeted antitumor drug delivery systems [7,8]. Under physiological pH, these polymers are typically deprotonated; however, under acidic conditions, they become protonated, causing structural deterioration of the material. This modification affects the hydrophobicity and facilitates drug release at acidic pH through the protonation of polymeric carboxylate groups [5]. Several pH-responsive polymers have been studied for drug delivery, such as poly(acrylic acid), poly(ethylene oxide), and poly(lactic-co-glycolic acid). The poly(methacrylic acid), or P(MAA), stands out, which is a typical example of a pH-sensitive polymer with weak acidic structural groups that protonate or deprotonate in response to environmental pH changes [9].

Although polymeric nanoparticles have been adopted as a method for delivering drugs in some studies, utilizing this material as a single phase for drug delivery systems remains a significant challenge. These materials are not mechanically resistant, especially to shear, the main type of mechanical stress to which materials suspended in the bloodstream [10]. As an alternative, the association of inorganic materials such as mesoporous silica appears as an alternative when combining the mechanical strength of the inorganic phase with the responsiveness of the organic one, thus giving rise to composites with broader applicability.

Mesoporous silica nanoparticles (MSN) have unique structural properties, such as biocompatibility, high specific surface area, adjustable pore size and well-defined surface properties [11]. Several studies of mesoporous silica combined with stimulus-responsive polymers have been described in the literature [12]. In addition to silica, reports on biomedical research also reveal hydroxyapatite (HA) as one of the most investigated treatments for bone-related cancers such as osteosarcoma [13,14], due to its biocompatibility and similarity with the bone mineral phase. Furthermore, these materials have osteoconductive and osteoinductive properties, which are desirable for bone regeneration therapies [15]. With the technological advances of the last decades, the need arises to develop sophisticated drug delivery systems that are more specific to the tumor microenvironment and that help in the diagnosis of cancer. Diagnosis is an essential procedure to understand the extent of tumor progression and may mean a relatively more effective way to treat early-stage disease [16]. Therefore, another interesting strategy involves the combination of therapy associated with luminescent elements for application in diagnostic imaging. Multifunctional systems with an emphasis on therapy and diagnosis simultaneously, known as theranostic systems, have shown promise in several studies [17]. Several luminescent agents such as rare earth elements have been explored for this application, due to the outstanding optical, magnetic and X-ray attenuation properties, as well as the radioactivity of its isotopes [18].

In a previous work developed by our research group, a pH-sensitive hybrid system composed of silica, hydroxyapatite and europium (MSN/HA-Eu), followed by polymerization of poly(methacrylic acid) hydrogel on the surface of nanoparticles. The experimental data showed a drug release profile of methotrexate dependent on the pH and luminescent potential of the obtained systems, encouraging the development of a new material [19]. Despite these findings, improvements in the luminescent signal are still needed for application in medical diagnostic imaging. Some studies show that increasing the intensity of luminescence based on energy transfer and electron transfer process between rare earth elements is an effective way. For example, XIE et al. (2016) used the transfer of energy from Gd^{3+} to Eu^{3+} as a strategy to improve the luminescence of HA nanoparticles doped with rare earths [20].

Given the above considerations, this work aimed to synthesize and characterize silica/hydroxyapatite hybrids nanocomposites co-doped with Eu and Gd functionalized with pH-

Preprints (www.preprints.org) | NOT PEER-REVIEWED | Posted: 19 May 2023 doi:10.20944/preprints202305.1385.v1

sensitive polymers to compose a multifunctional system MSN/HA-Eu(2%)-Gd(1%)/P(MAA) with multiple techniques. We also investigated the photoluminescent properties of this system, as well as its incorporation and release profiles of the antitumor drug doxorubicin (DOX) under different pH conditions.

2. Materials and Methods

2.1. Materials

Methotrexate, methacrylic acid (MAA) monomer, N,N,N′,N′-tetramethylenediamine (TEMED) monomer, tetraethyl orthosilicate (TEOS), hexadecyltrimethylammonium bromide (CTAB), calcium chloride ($CaCl_3$), dipotassium hydrogen phosphate trihydrate ($K2HPO4{\cdot}3H2O$), and gadolinium chloride hexahydrate (III) ($GdCl_3.6H_2O$) were purchased from Sigma-Aldrich. Triethylene glycol dimethacrylate (TEGDMA) monomer, ammonium persulfate (APS), ethanol, and europium oxide were purchased respectively from Fluka Chemie GmbH, VETEC Química Fina, Merck, and Specsol. Ammonium hydroxide and nitric acid were purchased from Synth.

2.2. Synthesis and Characterization

The experimental steps used in the development of the luminescent nanocomposite (MSN/HA-Eu(2%)-Gd(1%)) and the hybrid luminescent system (MSN/HA-Eu(2%)-Gd(1%)/P(MAA)) are summarized in the flowchart of Figure 1.

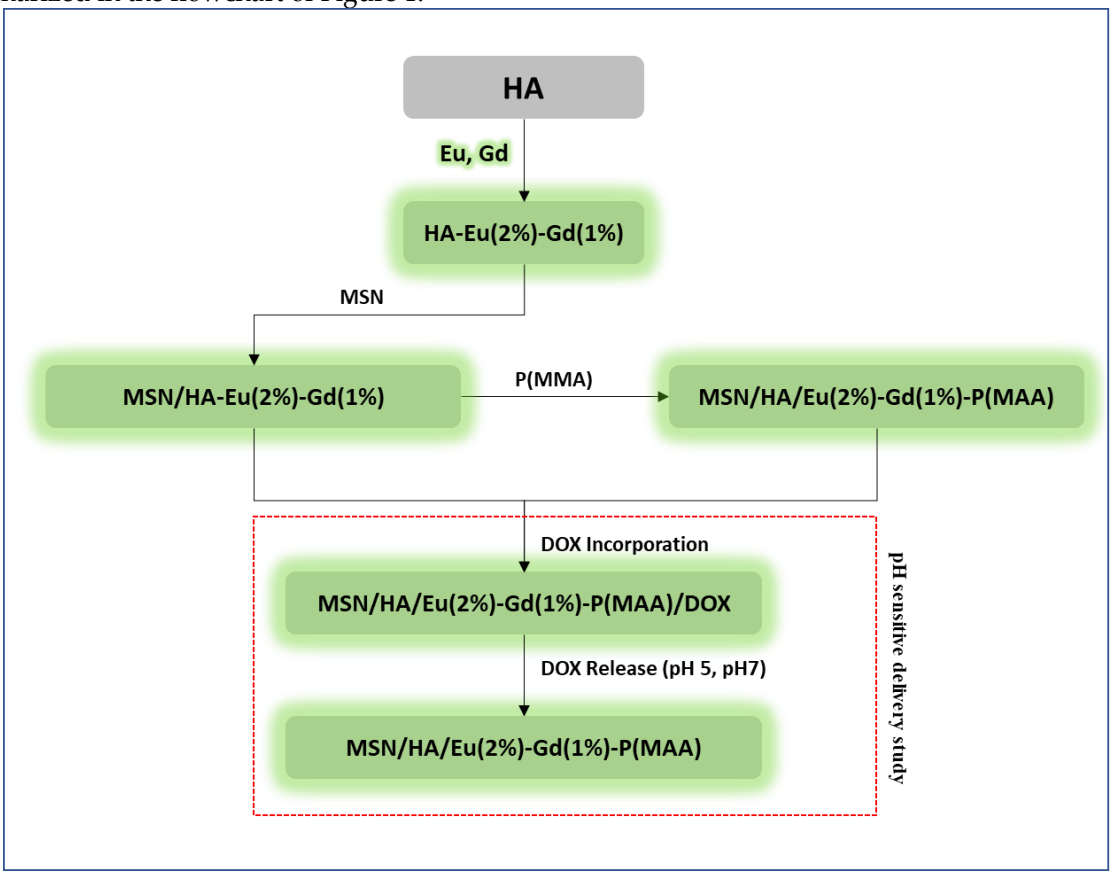

Figure 1. Flowchart with summary of all stages of synthesis and characterization of MSN/HA-Eu(2%)-Gd(1%) and MSN/HA-Eu(2%)-Gd(1%)/P(MAA) materials.

2.2.1. Synthesis of Eu^{3+}/Gd^{3+} Co-doped Hydroxyapatite (HA-Eu(2%)-Gd(1%))

The synthesis of the europium/gadolinium co-doped hydroxyapatite followed the described procedure in the literature [21] with modifications. The synthesis involves the preparation of two precursor solutions. Solution (I) was prepared by the complete dissolution of CTAB (2.8 g) in Milli-

Preprints (www.preprints.org) | NOT PEER-REVIEWED | Posted: 19 May 2023 doi:10.20944/preprints202305.1385.v1

Q® water under moderate stirring, followed by the addition of dipotassium hydrogen phosphate trihydrate (0.1 M) at pH 12. Solution (II) was prepared with 0.44 g of europium oxide (Eu_2O_3) in an aqueous solution of nitric acid (HNO_3) (1:5), kept at 78 °C giving rise to europium nitrate [$Eu_3(NO_3)_3$]. After this step, a calcium chloride solution (0.167 M) was added to the solution (II). The concentration of the precursors was kept at a ratio of 2% of Eu-doping and 1% of gadolinium (HA-Eu(2%)-Gd(1%)) relative to the amount of Ca^{2+}. Solution (II) was dropwise added to solution (I) and kept stirring for 24 h. After this, the resulting suspension underwent hydrothermal treatment at 100 °C for 24 h. The material was then filtered, washed, and dried at 60 °C. The remaining surfactant (CTAB) was removed by calcination at 575 °C, resulting in a fine whitish powder. For comparison, the HA nanoparticles were obtained through this same chemical route, but without the addition of europium nitrate and gadolinium chloride hexahydrate (III) ($GdCl_3.6H_2O$).

2.2.2. Synthesis of MSN/HA-Eu(2%)-Gd(1%) system

The MSN/HA-Eu(2%)-Gd(1%)]system was synthesized following the methodology applied in the HA-Eu(2%)-Gd(1%) sample synthesis, adding one more step after the end of solution (II) addition, when 14 mL of TEOS was added to the system [22]. After 14 h, the resulted suspension was thermal treatment at 100 °C for 24 h. The subsequent steps were the same as in the previous sample. For comparison, the MSN/HA nanocomposite was obtained through this same chemical route, but without the addition of europium and gadolinium salts. The Figure 2 shows a schematic representation of the of synthesis of MSN/HA-Eu(2%)-Gd(1%) system.

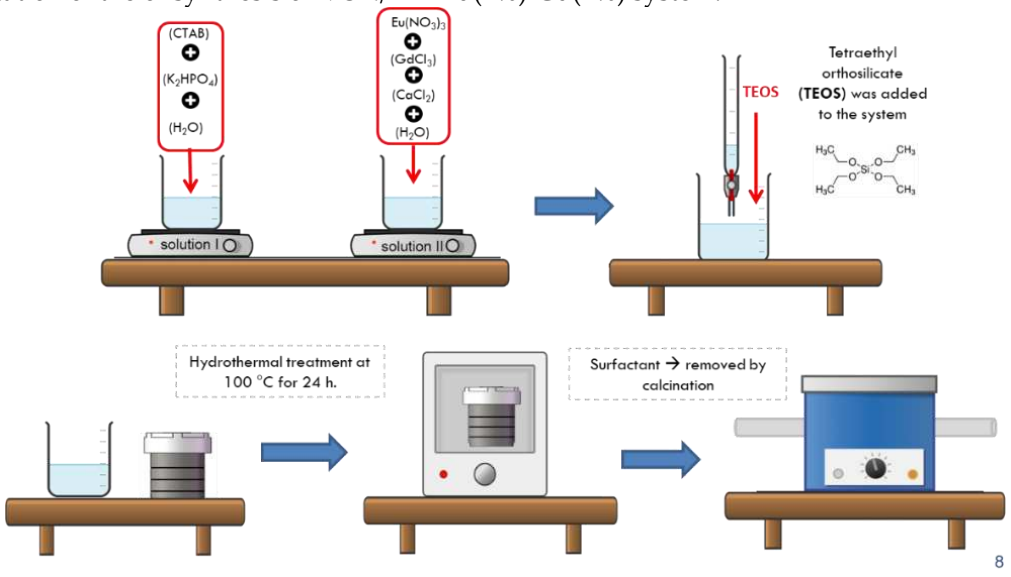

Figure 2. Schematic representation of the synthesis of Eu-doped silica/hydroxyapatite nanocomposites (MSN/HA-Eu(2%)-Gd(1%)).

2.2.3. Synthesis of the Hybrid System: MSN/HA/Eu(2%)-Gd(1%)-/P(MAA)

The poly(methacrylic acid) polymerization process in the nanocomposite structures was carried out to obtain a hybrid material with pH-sensitive characteristics for drug delivery systems. For this purpose, the TEGDMA crosslinking agent was diluted in a 40% ethanol solution and used during the polymerization reaction of the MAA monomer to form three-dimensional crosslinks in the polymeric chains around the nanoparticles. The MAA monomer (492.6 µL) was diluted in a NaOH solution (2.0 M), followed by the addition of the Eu-Gd-doped nanocomposite (0.2 g) and the TEGDMA/ethanol solution. The system was cooled to 10 °C. Subsequently, the TEMED activator (16 µL) and ammonium persulfate initiator (0.0125 mg) were added under constant nitrogen flow. The system was kept under agitation in a bath at 10 °C for 72 h and the material obtained was centrifuged, washed, and dried. For comparison, the MSN/HA nanocomposite, without doping (Eu,Gd), was also obtained with P(MAA) following the same methodology.

 doi:10.20944/preprints202305.1385.v1

2.2.4. Characterization of Materials

The structural analysis of the synthesized materials was performed by X-ray diffraction (DRX - Ultima IV, Rigaku Inc., Japan) with Cu Kα radiation (λ = 0.154 nm). The 2-theta varies from 10º to 80º with a step size of 0.02º and a scanning rate of 2º min^{-1}. Possible alterations in the HA crystal lattice caused by the presence of Eu and Gd were investigated through the Rietveld refinement [23]. In this study, the network parameters and dimensions of the unit cell were determined, with the help of the FullProf software [24]. Chemical bonds and functional groups of the materials obtained were analyzed using a Fourier transform infrared spectroscopy (FT-IR, Thermo Nicolet 6700). The absorbance was in the range of 4000 and 400 cm^{-1}. The textural characterization was achieved by N_2 adsorption in an Autosorb iQ gas sorption analyzer (Quantachrome Instruments, USA); data acquisition, calculation, and reporting were processed by the Quantachrome ASiQwin™ software. The specific surface area was calculated though Brunauer- Emmett-Teller method, from 0.05 to 0.35 P/P_0, while pore volume and pore sizes were calculated using the Barret-Joyner-Halenda (BJH) theory applied on N_2 desorption data from the obtained isotherms; all the samples analyzed were outgassed for 48 h at 40 °C. The morphology of the materials was analyzed by scanning electron microscopy (SEM - Σigma VD series, ZEISS, Germany) and transmission (TEM - Tecnai G2-12 SpiritBiotwin, FEI Company, USA). The photoluminescence (PL) spectra were obtained with a UV-VIS USB 2000 (Ocean Optics) spectrometer; samples were excited at room temperature with a 457 nm wavelength laser, MODU-LASER Stellar Pro Multi-Line 150 mW. Magnetic characteristics of the samples were performed by vibrational sample magnetometry (VSM e 7400 series, LakeShore Cryotronics, USA). The Zeta potential of the samples was investigated using the Nanozetasizer Zs equipment (Malvern Instruments, United Kingdom). The measurements were carried out at a temperature of 25ºC. For analysis, samples were dispersed in Milli-Q® water at a concentration of 0.1 $mg.mL^{-1}$ in a tip ultrasound with an energy of 15 kJ. The measurements were carried out in a nitrogen atmosphere with a flow rate of 50 mL min^{-1}. Elemental analysis was used to quantify the carbon, hydrogen and nitrogen contents in the samples and was conducted in the EA 2400 Series II CHNS/O equipment from PerkinElmer, using 2-3 mg of material.

2.2.5. Doxorubicin Incorporation and Releasing Assays

The DOX incorporation was carried out by incubating the hybrid MSN/HA-Eu(2%)-Gd(1%)/P(MAA) nanocomposite (25 mg) in a doxorubicin solution (0.75 mg mL−1) for 72 h under vigorous and constant stirring at room temperature. The suspension was filtered, and the sample washed and dried for 24 h. The drug concentration in the passing liquid was measured in a UV-2550 UV-Vis spectrometer (Shimadzu, Japan), making it possible to calculate the drug encapsulation. The same drug loading process was applied to the MSN/HA-Eu(2%)-Gd(1%) nanocomposite for comparison.

The in vitro (DOX) release behavior was investigated as a function of time. The drug release tests were conducted to study the release kinetics of DOX from hybrid system and nanocomposite matrices in acetate buffer solution (pH 5) and PBS (pH 7). The DOX-loaded samples (6,5 mg) were put into a dialysis membrane (D9277 - Sigma-Aldrich) and incubated in buffer solutions at 37 °C under continuous stirring at a rate of 50 rpm. The released DOX levels were measured in the buffer solutions by UV-Vis spectrometry at 233 nm.

3. Results and Discussion

3.1. X-ray Diffraction (XRD)

The synthesized materials were investigated using the X-ray diffraction technique. In order to evaluate possible impacts on the formation of hydroxyapatite, caused by co-doping with europium and gadolinium, results of materials synthesized only with europium (HA-Eu(2%) and MSN/HA-Eu(2%)) will also be presented, for purposes of comparison.

Preprints (www.preprints.org) | NOT PEER-REVIEWED | Posted: 19 May 2023 doi:10.20944/preprints202305.1385.v1

The results evidenced reflection peaks in all the diffractograms that can be assigned to the hexagonal hydroxyapatite crystalline phase with spatial group P63/m, according to the card number 9-432 from Powder Diffraction File database (PDF2, International Centre of Diffraction Data—ICDD) as shown in Figure 3. The characteristic peaks at 32°, 33°, and 34° Bragg angles (2θ) can be respectively attributed to the (211), (300), and (202) crystallographic planes, in agreement with the literature [25]. Similar work described in the literature also showed the formation of HA phase, confirmed due to the appearance of characteristic patterns in the Bragg angles [21,26].

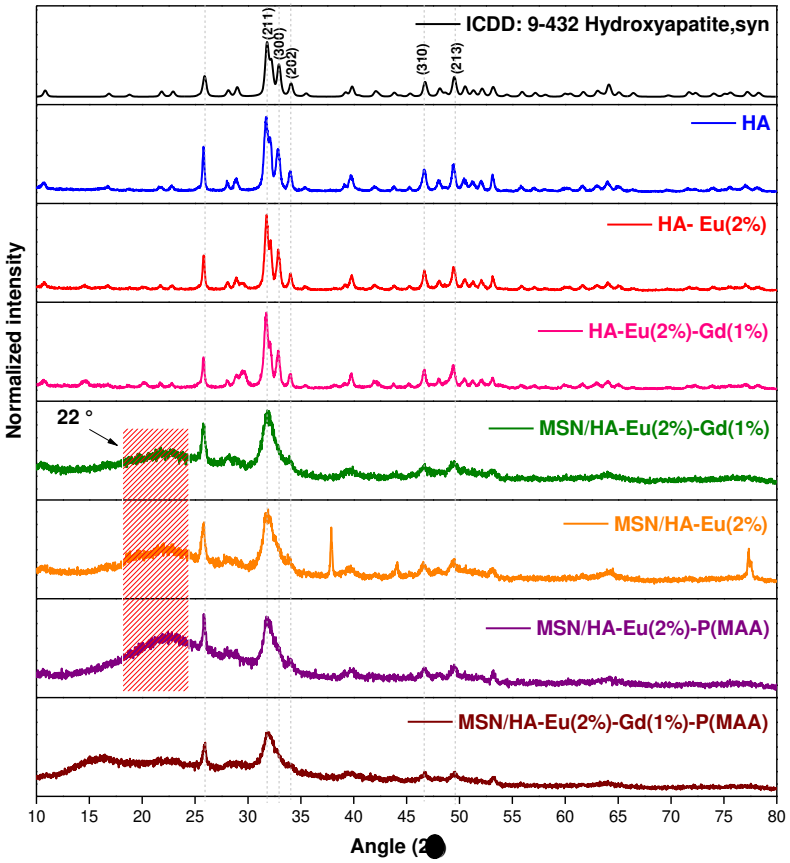

Figure 3. X-ray diffractograms for ICDD:9-432 hydroxyapatite and HA, HA-Eu(2%), HA-Eu(2%)-Gd(1%), MSN/HA-Eu(2%), MSN/HA-Eu(2%)-Gd(1%), MSN/HA-Eu(2%)/P(MAA) and MSN/HA-Eu(2%)-Gd(1%)/P(MAA).

The MSN/HA-Eu(2%), MSN/HA-Eu(2%)-Gd(1%), MSN/HA-Eu(2%)/P(MAA) and MSN/HA-Eu(2%)-Gd(1%)/P(MAA) samples revealed a diffuse halo in the 15° to 35° 2θ range (Figure 3, the broad peak centered around 22°), which can be assigned to the characteristic short-range periodicity of the $(SiO4)^{4-}$, a tetrahedral unit of amorphous silica nanoparticles suggesting that the synthesis of the nanocomposites was successfully achieved. This finding is in agreement with previous works in the literature [19].

Figure 4 compares XRD results of the HA, HA-Eu(2%) and HA-Eu(2%)-Gd(1%) samples. The results show that the HA-Eu(2%) and HA-Eu(2%)-Gd(1%) samples showed a small peak at the Bragg angle 2θ of approximately 29º (Figure 4a). This peak can be attributed to the presence of a second phase after the doping processes, confirmed by the Rietveld refinement, as shown in Figure 4b–d and Table 1. For HA-Eu(2%) and HA-Eu(2%)-Gd(1%) samples, it is observed that there was the formation of a secondary phase of $Ca_2P_2O_7$, which corresponds, respectively, to 8.3% and 25.5% of the synthesized material. Despite this, these materials are mainly composed of the hydroxyapatite phase, as shown in Table 1. Therefore, the XRD result indicates the synthesis of crystalline materials with HA as the primary phase in the dopant materials.

Preprints (www.preprints.org) | NOT PEER-REVIEWED | Posted: 19 May 2023 doi:10.20944/preprints202305.1385.v1

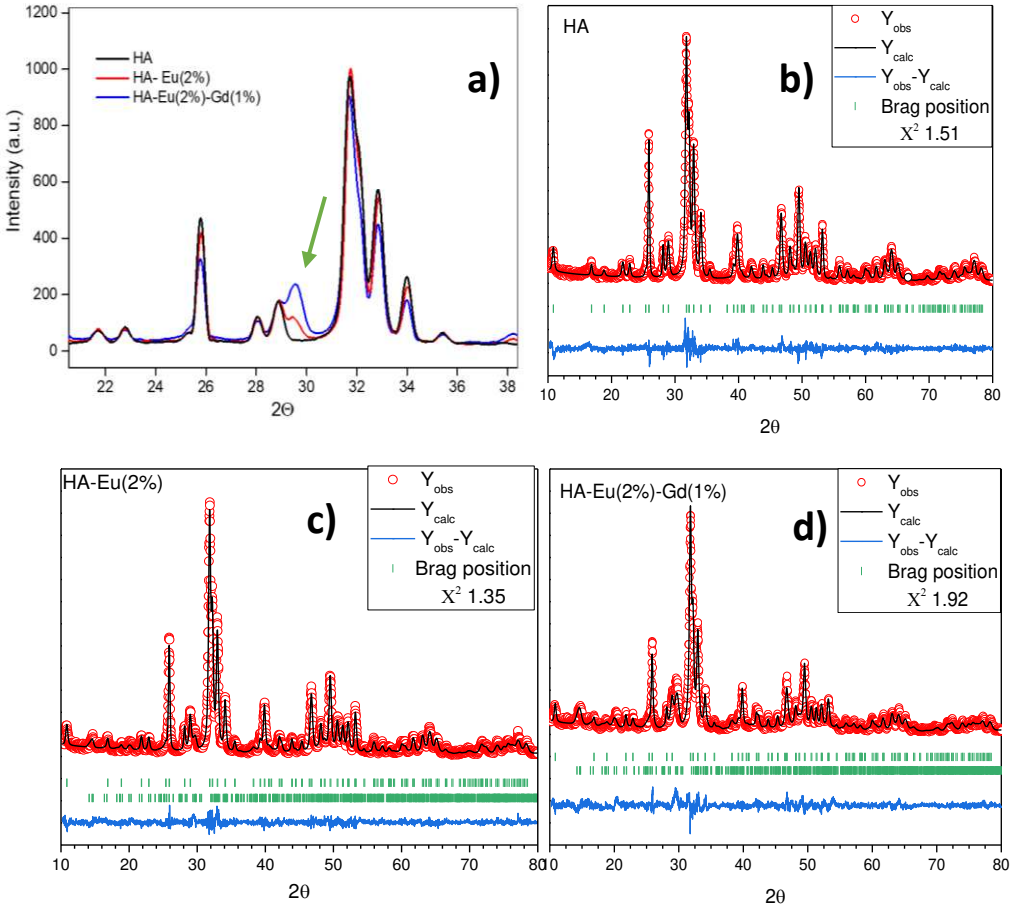

Figure 4. (**a**) XRD results of the HA, HA-Eu(2%) and HA-Eu(2%)-Gd(1%) samples. Diffraction patterns with Rietveld refinement of the: (**b**) HA (**c**) HA-Eu(2%) and (**d**) HA-Eu(2%)-Gd(1%) samples. The observed and calculated data are represented by the stars and solid lines, respectively.

The results show good agreement with the reference values (ICSD16742). A decrease in the unit cell volume is observed in all synthesized materials in relation to the reference value (530.139 Å^3). Different values of this parameter are found in the literature ranging from 525.580 Å^3 to 532.48 Å^3 [27,28]. Aldén and collaborators suggest that these variations can be attributed mainly to the presence of contaminants, such as carbonates and fluorides, which can occupy the positions of Ca and the phosphate group in the unitary cell of hydroxyapatite [27]. Furthermore, the addition of rare earths into the hydroxyapatite structure resulted in reduced mean grain size (Table 1). This may occur due to the decreasing of Ca-O distances and smaller ionic radius for rare earths resulting in a reduction of cell parameters as shown in Table 1 [29–31].

Table 1. Table. Parameters obtained from the Rietveld refinement of XRD: The mean grain size (<D>), lattice parameters (a, b, c and V) and S=Rwp/Rexp, parameter that quantifies the quality of the refinement.

Sample		Cell parameters							
		a (Å)	*b* (Å)	*c* (Å)	*V* (Å^3)	Space group	<*D*> (nm)	Phase content (%)	*S*
Standard (ICSD) 16742	HA	9.43200	9.43200	6.88100	530.1	*P6$_3$/m*	----		

Preprints (www.preprints.org) | NOT PEER-REVIEWED | Posted: 19 May 2023 doi:10.20944/preprints202305.1385.v1

HA	HA	9.4222 (1)	9.4222 (1)	6.8854 (1)	529.3 (1)	*P6₃/m*	28.4 (8.4)	100 (0)	1.23
HA-Eu(2%)	HA	9.4125 (1)	9.4125 (1)	6. 8820 (1)	528.0 (1)	*P6₃/m*	22.6 (0.2)	91.7 (0.5)	1.16
	$Ca_2P_2O_7$	11.7711 (1)	7.7763 (1)	10.8376 (1)	893.2 (1)	*P 2₁/c*		8.3 (0.2)	
HA-Eu(2%)-Gd(1%)	HA	9.4169 (1)	9.4169 (3)	6.8866 (1)	528.9 (1)	*P6₃/m*	22.2 (6.1)	76.0 (0.5)	1.38
	$Ca_2P_2O_7$	11.7914 (1)	7.6631 (1)	10.9040 (1)	887.2 (1)	*P 2₁/c*		24.0 (0.3)	

3.2. Fourier Transform Infrared Spectroscopy (FTIR)

Figure 5 shows the FTIR spectra for HA, HA-Eu(2%)-Gd(1%), MSN/HA-Eu(2%)-Gd(1%) and MSN/HA-Eu(2%)-Gd(1%)/P(MAA). The spectra evidence the presence of hydroxyapatite in all the samples, due to the characteristic transmittance of the phosphate (1098–1037, 960, 603, 560, and 470 cm^{-1}) and hydroxyl stretching (3571 and 638 cm^{-1}) [19,26,32]. The bands observed around 1454– 1412 cm^{-1} in the HA and HA-Eu(2%)-Gd(1%) spectra can be attributed to the carbonate (CO_3^{2-}) vibrational modes. These ions may have originated due to the exposure of these samples to atmospheric CO_2 before the hydrothermal treatment or due to the decomposition of the CTAB during the calcination process [21,26].

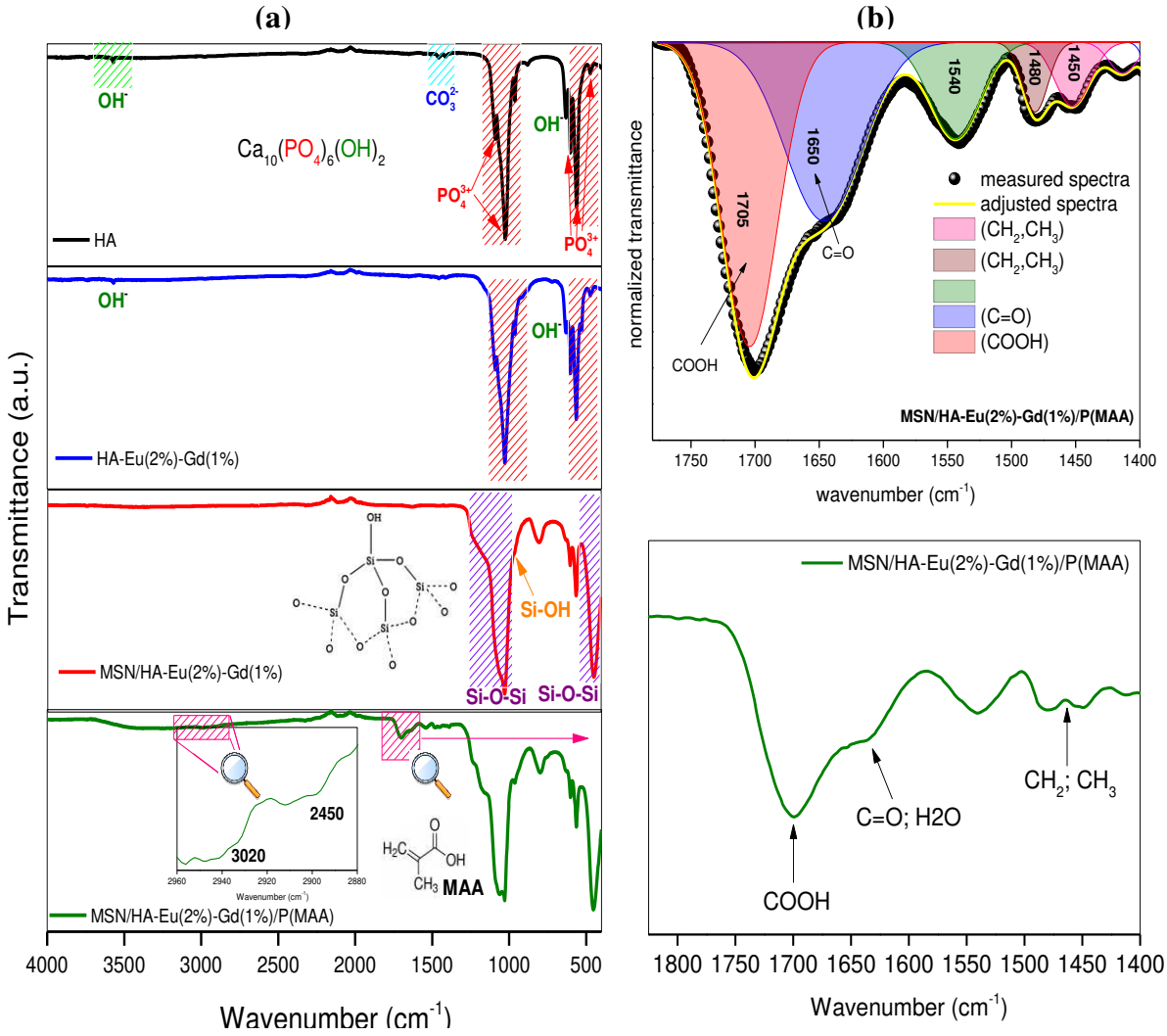

 doi:10.20944/preprints202305.1385.v1

Figure 5. (**a**) FTIR spectra of HA, HA-Eu(2%), HA-Eu(2%)-Gd(1%), MSN/HA-Eu(2%), MSN/HA-Eu(2%)-Gd(1%), MSN/HA-Eu(2%)/P(MAA) and MSN/HA-Eu(2%)-Gd(1%)/P(MAA) samples (**b**) deconvolution of normalized FTIR spectra of MSN/HA-Eu(2%)-Gd(1%)/P(MAA).

FTIR spectra of MSN/HA-Eu(2%)-Gd(1%) and MSN/HA-Eu(2%)-Gd(1%)P(MAA) samples present the typical MSN vibrational modes. The characteristic transmittance bands from the angular deformation mode of Si-O-Si bonds can be found around 464 cm^{-1} [33,34], the Si-O symmetrical stretching mode is located at 810 cm^{-1} [34], the Si-OH stretching mode at 961 cm^{-1} [35], and the a symmetric stretching of Si-O-Si bonds around 1075 a 1224 cm^{-1} [36]. The presence of the characteristic bands of MSN and HA in the FTIR spectra of the nanocomposites suggests that mesoporous silica can be formed in the hydroxyapatite nanoparticles, in agreement with the XRD results.

The presence of functional groups related to the polymeric phase is noted. The peaks around 3020 and 2450 cm^{-1} (Figure 4a) are attributed to the symmetrical and asymmetrical stretching modes of the -CH_2 and CH_3 groups, which arose due to the incorporation of the polymer phases [10,37]. In the deconvolution of region of 1750-1400 cm^{-1} (Figure 4b), it becomes evident a band around 1650 cm^{-1} that can be attributed to the stretching modes of the carbonyl groups (C=O) present in the monomer [38,39]. The band between 1700 and 1715 cm^{-1} can be related to the characteristic stretching modes of the carboxylate group, which is part of the MAA monomer used during polymerization, reinforcing the evidence of the presence of the polymeric phase in the hybrid [19,40]. These bands have already been observed by other works in studies involving nanoparticles to which polymeric phases have been incorporated [10,19].

Figure 6 shows the FTIR spectra obtained for the samples MSN/HA-Eu(2%)-Gd(1%) and MSN/HA-Eu(2%)-Gd(1%)/P(MAA) to which the antitumor drug DOX were incorporated. The bands already observed for these materials prior to the incorporation of the drugs continued to be observed, indicating the maintenance of the phases of the materials even after the entire incorporation process. Furthermore, typical doxorubicin bands were identified in the sample spectra indicating that drug incorporation process was achieved. The bands at 3340 cm^{-1} N–H (3525 cm^{-1}), O-H (2987 cm^{-1}), C–H (2897 cm^{-1}), C=O (1720 cm^{-1}), C=C ring (1690, 11581 and 1540 cm^{-1}), C–O–C (1071 cm^{-1}), C=H bend, C=C ring bend (800 cm^{-1}) can be interpreted as indicative of the presence of the drug in these samples [41,42].

Preprints (www.preprints.org) | NOT PEER-REVIEWED | Posted: 19 May 2023 doi:10.20944/preprints202305.1385.v1

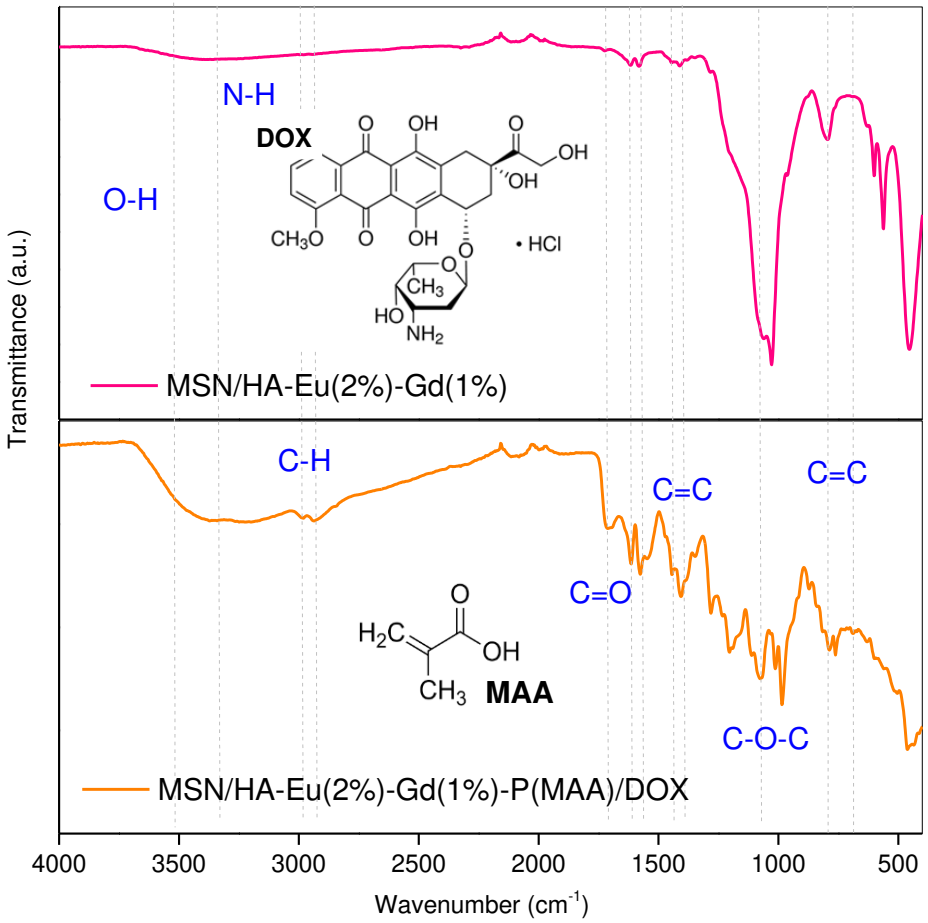

Figure 6. FTIR the samples MSN/HA-Eu(2%)-Gd(1%) and MSN/HA-Eu(2%)-Gd(1%)/P(MAA) to which the antitumor drug DOX were incorporated.

3.3. Scanning Electron Microscopy (SEM) and Transmission Electron Microscopy (TEM)

The morphological and structural characterization of the nanoparticles was performed by SEM and TEM techniques. The images of HA (Figure 7a), and HA-Eu(2%)-Gd(1%) (Figure 7b) showed a trend towards the formation of nanorods as a contribution of the presence of HA in a well-agglomerated form [19]. The rod-like shape of the hydroxyapatite nanoparticles can be understood as a result of the anisotropic growth of the HA nanocrystals along the c-axis direction [43]. This result indicates that the presence of dopants does not promote significant changes in the morphology of the material. The nanorods morphology was also observed in the TEM images of the samples containing dopants (Figure 7 e,f).

Preprints (www.preprints.org) | NOT PEER-REVIEWED | Posted: 19 May 2023 doi:10.20944/preprints202305.1385.v1

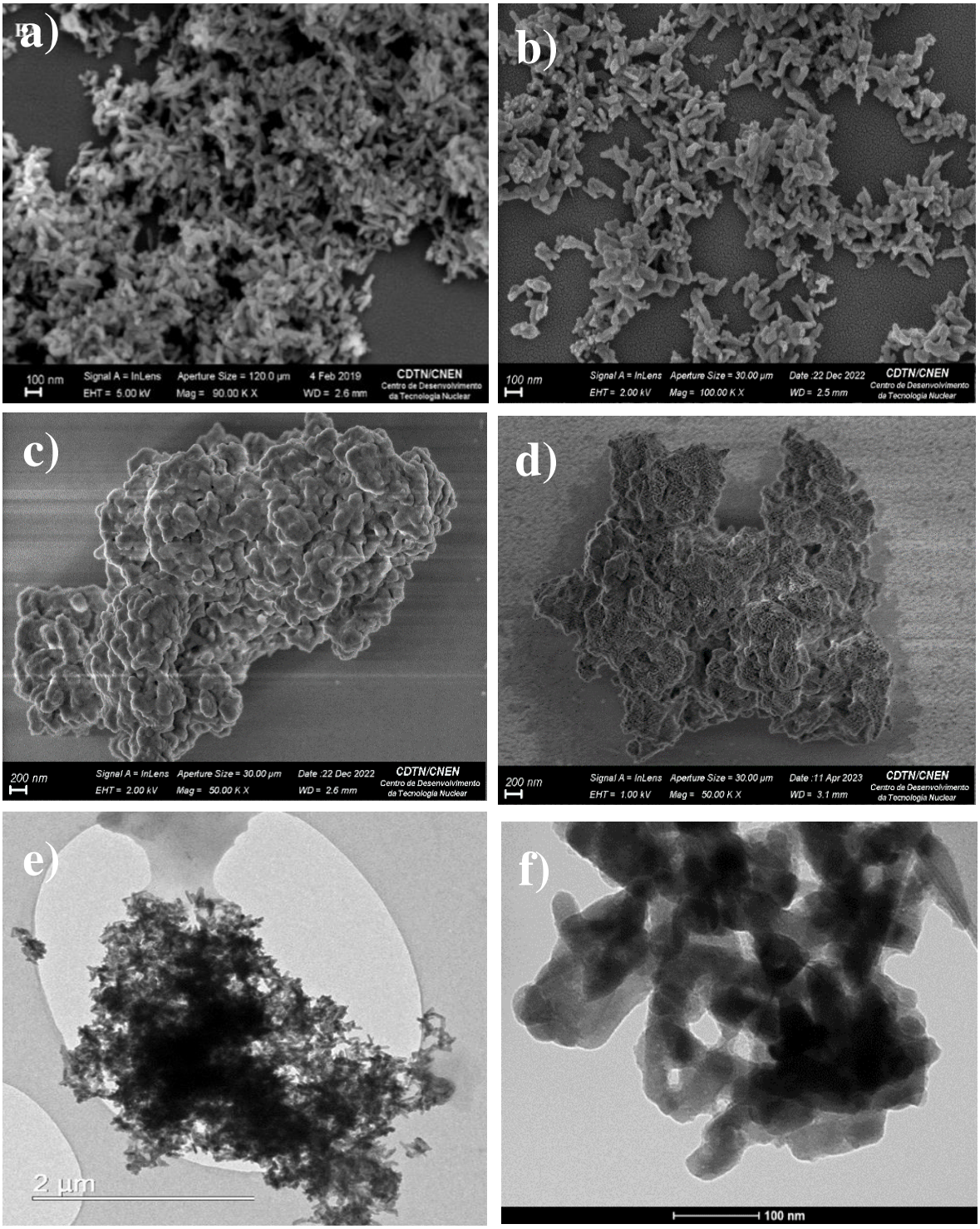

Figure 7. MEV of (**a**) HA (**b**) HA-Eu(2%)-Gd(1%) (**c**) MSN/HA-Eu(2%)-Gd(1%) (**d**) MSN/HA-Eu(2%)-Gd(1%)/P(MAA). TEM of (**e**) HA and (**f**) HA-Eu(2%)-Gd(1%).

In addition, it is noticed that the silica altered the aspect of the nanoparticles when compared to the samples of HA and HA-Eu(2%)-Gd(1%). The results show a more rounded morphology with some heterogeneity between them as shown in Figure 7c,d [19,44]. It is known that pure silica nanoparticles tend to form nanospheres when synthesized in a basic medium and in the presence of CTAB [11]. These results show that particles present an average diameter of less than 200 nm. This size range is desirable in candidate nanomaterials to act in cancer treatment by the enhanced

 doi:10.20944/preprints202305.1385.v1

permeability and retention effect (EPR) because the accumulation of nanoparticles on tumor sites may be favored by the nanoscale of the porosity of blood vessels common in tumors [45].

3.4. Potential Zeta (ζ)

The zeta potential is used to characterize the surface charges of the particles and the values obtained are presented in Table 2. The results obtained indicate a value around -17 mV for HA, which is attributed to the ionization of the hydroxyl groups (OH) present in the surface of the material, a result that agrees with the load presented by most of the hydroxyapatite ceramics in the literature [46,47]. After the doping process with Eu and Gd, there is no significant difference in the Zeta potential. This fact can be explained by the HA unit cell that has calcium in two positions, a more internal and another more external atom in relation to their structure. Therefore, the doping process may have occurred in the most internal positions of the unit cell, not being detected by this technique. The presence of silica in the system caused a decrease in the Zeta potential (-23.2 ± 0.23). Probably, this result may be related to the presence of negative charge on the surface of this material due to the presence of silanol groups characteristic of this material [48]. After polymerization with methacrylic acid, an increase in the negative value of zeta potential is observed, probably due to the presence of carboxyl groups [37]. Furthermore, the Zeta potential of the hybrid sample changed from -27.2 mV to -21.0 mV after the drug incorporation process. Possibly, the amino group present in doxorubicin may have contributed to the decrease in the negative charge of the MSN/HA-Eu(2%)-Gd(1%)/P(MAA)-DOX system, allowing us to suggest that DOXO was incorporated into the material. This result is in line with what was observed in the FTIR.

Table 2. Zeta Potential of HA, HA/Eu(2%)-Gd(1%), MSN/HA/Eu(2%)-Gd(1%) and MSN/HA/Eu (2%)-Gd(1%)/P(MAA).

Samples	Zeta Potencial ± SD (mV)
HA	-16.8 ± 0.23
HA/Eu (2%)-Gd(1%)	-15.0 ± 0.55
MSN/HA/Eu(2%)-Gd(1%)	-23.2 ± 0.23
MSN/HA/Eu (2%)-Gd(1%)/P(MAA)	-27.2 ± 0.80
MSN/HA/Eu(2%)-Gd(1%)-DOX	-17.8 ± 0.56
MSN/HA/Eu (2%)-Gd(1%)/P(MAA)/DOX	-21.0 ± 0.23

The zeta potential helps evaluate the stability of colloidal dispersions. In drug delivery systems, the zeta potential measurements help optimize the stability and performance of drug delivery systems. It assists in determining the surface charge and stability of these systems, which can affect their circulation time, interaction with cells, and drug release behavior. The ideal zeta potential value for a controlled drug delivery system can vary depending on various factors, including the specific formulation, the intended mode of action, and the target site within the body [6]. However, in general, a moderately high zeta potential (either positive or negative) is often preferred for controlled drug delivery systems. In general, the margin that defines the stability of colloidal suspensions is -30 mV and +30 mV, where the higher the zeta potential values, in modulus, the more stable the suspensions. It is observed that HA and HA/Eu (2%)-Gd(1%) materials present values a little different from these in modulus, suggesting that these materials do not present high stability in colloidal suspensions. It is observed that the addition of silica increased the value in modulus of the zeta potential in the MSN/HA-Eu(2%)-Gd(1%) sample. Nevertheless, the value presented by this material is still a little far from the ideal value. After the polymerization process with P(MAA), the zeta potential value obtained was -27.2. This appears as a promising result and shows that the presence of the polymer in the system can minimize the tendency to agglomeration and, consequently, improve the stability of the material. In this sense, to determine the stability of nanoparticles in aqueous dispersion, measurements of zeta potential were carried out over 15 days. Figure 8 presents the results of this

Preprints (www.preprints.org) | NOT PEER-REVIEWED | Posted: 19 May 2023 doi:10.20944/preprints202305.1385.v1

study through the distribution curves of zeta potential measurements for the different synthesized systems.

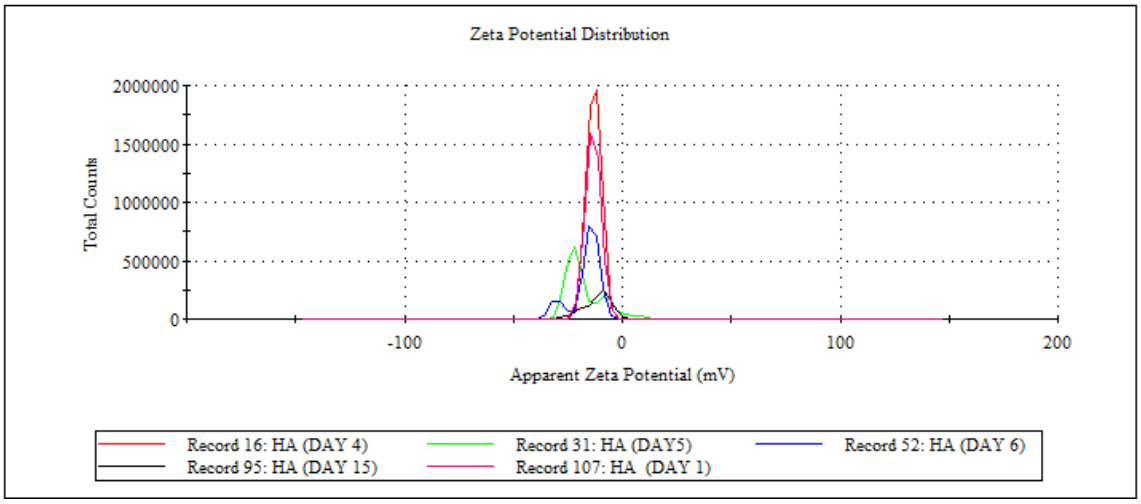

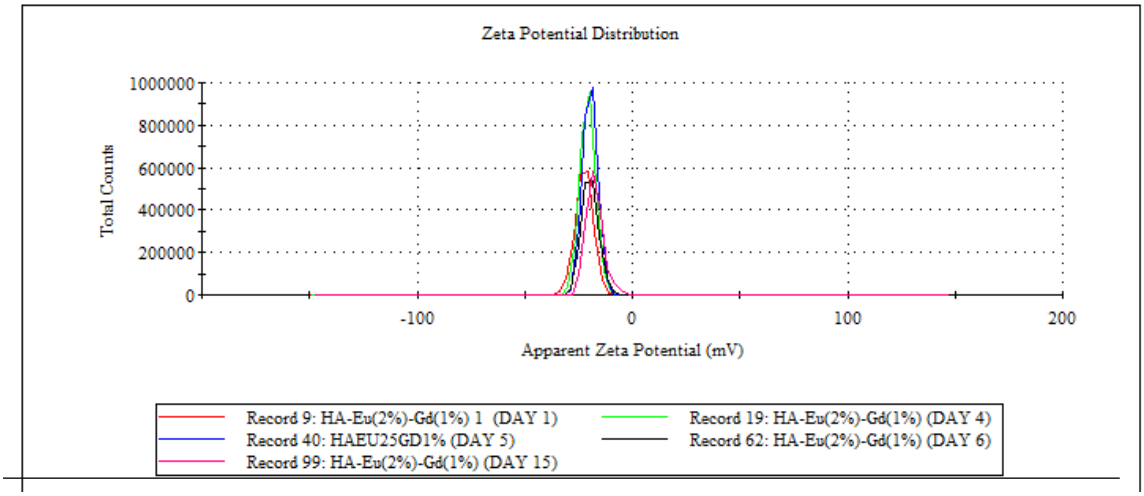

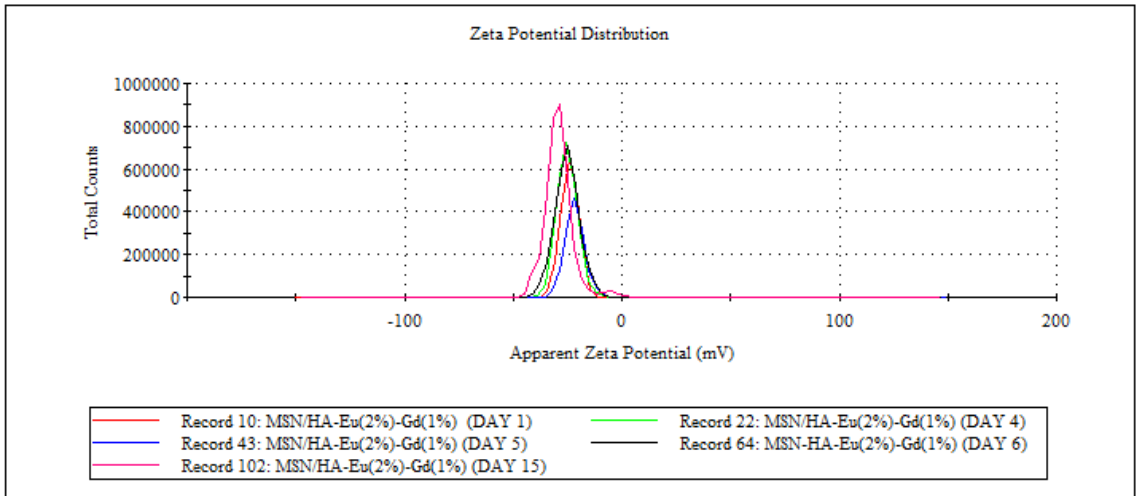

Preprints (www.preprints.org) | NOT PEER-REVIEWED | Posted: 19 May 2023 doi:10.20944/preprints202305.1385.v1

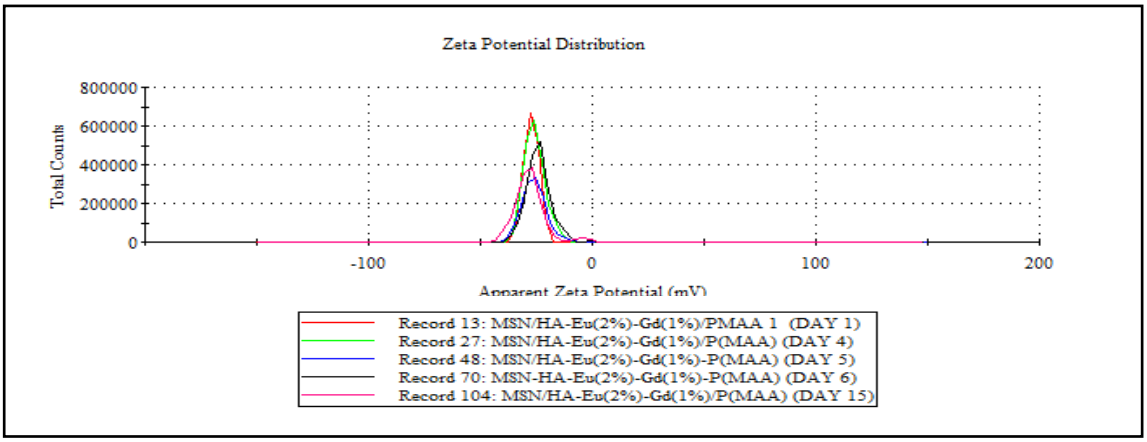

Figure 8. Distribution curves of zeta potential obtained for the samples HA, HA-Eu(2%)-Gd(1%), MSN/HA-Eu(2%)-Gd(1%) e MSN/HA-Eu(2%)-Gd(1%)/P(MAA) in different times.

Hydroxyapatite, when in aqueous dispersion, showed an altered surface charge throughout the studied period, indicating that the dispersion presents high instability over time, as expected for this system. In the results obtained for the HA-Eu(2%)-Gd(1%) system, it is observed that the nanoparticles doped with europium and gadolinium presented greater stability over 15 days in aqueous dispersion. The material remained stable with the same zeta potential distribution indicating that there was no significant change in the surface charge of the material during the analyzed period. In contrast, the MSN/HA-Eu(2%)-Gd(1%) nanocomposite showed some instability in the zeta potential value. Despite this, it is observed that after the polymerization process on the surface of this material, there was an improvement in the stability of these particles over 15 days. The hybrid system MSN/HA-Eu(2%)-Gd(1%)/P(MAA) maintained the zeta potential distribution over the 15 days. These data reinforce the need for a polymerization process to obtain a more stable material. The stability of this material is essential for a better application performance in biological systems.

3.5. CHN Elemental Analyses

Elemental analysis was used to quantify the presence of the elements carbon (C), hydrogen (H) and nitrogen (N) after the polymerization process and incorporation of the drug doxorubicin. This technique allows quantifying these processes through the percentage increase of these elements, compared to the inorganic matrix. The results obtained for the samples MSN/HA-Eu(2%)-Gd(1%), MSN/HA-Eu(2%)-Gd(1%)/P(MAA), MSN/HA-Eu(2 %)-Gd(1%)/DOX and MSN/HA-Eu(2%)-Gd(1%)/P(MAA)/DOX are shown in Table 3.

Table 3. Elemental analysis results.

Sample	C (%)	H (%)	N (%)
MSN/HA-Eu(2%)-Gd(1%)	0.33	0.59	0.33
MSN/HA-Eu(2%)-Gd(1%)/P(MAA)	24.10	4.05	1.05
MSN/HA-Eu(2%)-Gd(1%)/DOX	17.20	2.13	1.15
MSN/HA-Eu(2%)-Gd(1%)/P(MAA)/DOX	31.93	4.19	1.53

The MSN/HA-Eu(2%)-Gd(1%) sample showed low carbon contents (0.3%), possibly due to residual CTAB surfactant. The carbon content of the MSN/HA-Eu(2%)-Gd(1%)/P(MAA) (24.10%) sample increased in relation to the inorganic sample, indicating that the hybrid system was formed successfully, according to the FTIR results. In addition, samples loaded with the drug doxorubicin MSN/HA-Eu(2%)-Gd(1%)/DOX and MSN/HA-Eu(2%)-Gd(1%)/P(MAA)/DOX show a significant increase in carbon levels, confirming drug incorporation, according to FTIR results. There was no significant change in the percentage of nitrogen considering the measurement error.

Preprints (www.preprints.org) | NOT PEER-REVIEWED | Posted: 19 May 2023 doi:10.20944/preprints202305.1385.v1

3.6. N_2 Adsorption

Nitrogen adsorption and desorption isotherms of the HA-Eu(2%)-Gd(1%), MSN/HA-Eu(2%)-Gd(1%) and MSN/HA-Eu(2%)-Gd(1%)/P(MAA) samples are shown in Figure 9. This technique was used to evaluate the pore structure of samples, since the performance of the nanomaterial in controlled drug delivery is largely influenced by its pore structure.

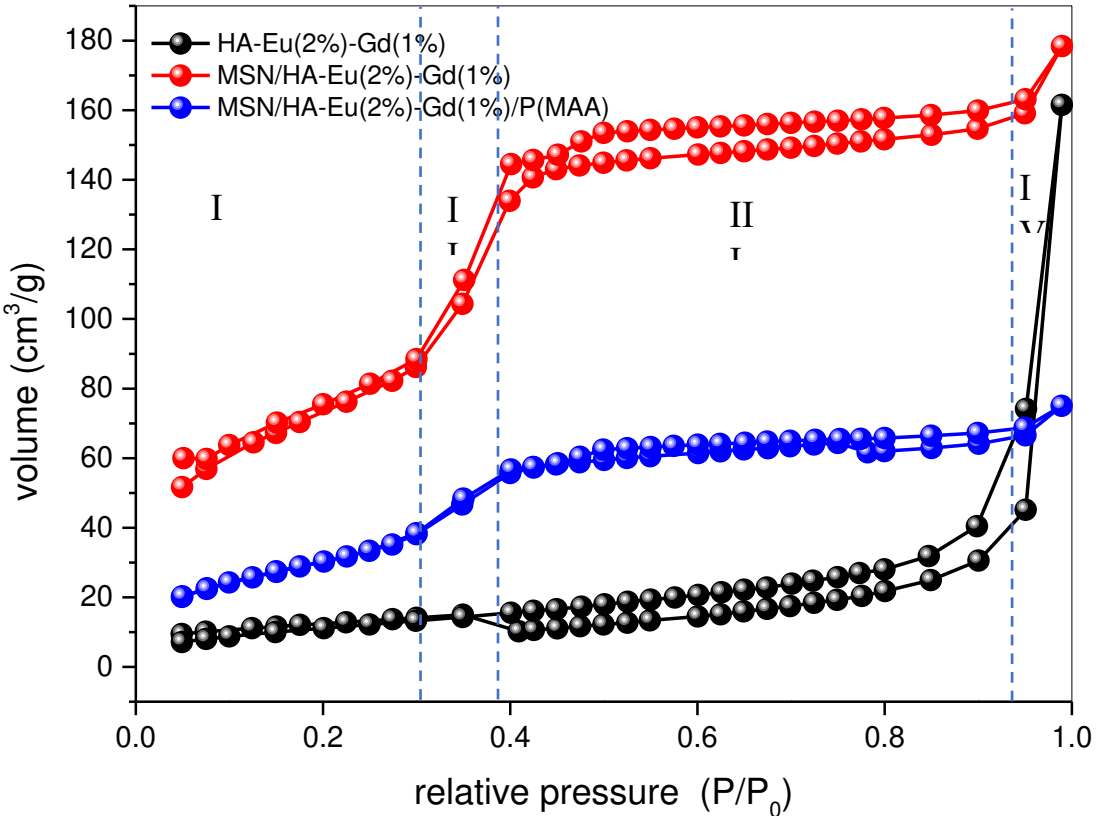

Figure 9. N_2 adsorption of HA-Eu(2%)-Gd(1%), MSN/HA-Eu(2%)-Gd(1%) and MSN/HA-Eu(2%)-Gd(1%)/P(MAA) samples.

It is possible to observe that sample MSN/HA-Eu(2%)-Gd(1%) and MSN/HA-Eu(2%)-Gd(1%)/P(MAA) samples exhibited type IV isotherms typical for mesoporous structures with constant cross-section porosity (cylindrical or hexagonal) and three-dimensionally ordered pores with lower or no blockage [19,46]. Four well-defined regions can be seen in these isotherms. Initially, in region I, a linear increase of the adsorbed volume happened due to the monolayer and multilayer adsorption on the surface of the material, including the surface of the mesoporous. In region II, the increase of the adsorbed volume at intermediate relative pressures was attributed to the capillary condensation phenomenon in the mesopores. In this point, the amount of adsorbed gas increased sharply with a small change in pressure due to the condensation of the adsorbate molecules below their vapor pressure. The adsorbate in the liquid state filled up the primary mesopores until the point in which the slope of the curve change, almost forming plateau. In region III, the increase in the adsorbed volume under high relative pressures was associated with the multilayer adsorption and/or to the condensation of the liquid in the secondary mesopores. Finally, in IV, the increase of the adsorbed volume corresponded to the filling of the voids between the particles that can be considered as porosity.

In sample HA-Eu(2%)-Gd(1%) it was possible to observe a sudden increase in the curves for high relative pressures. The abrupt increase in the adsorbed volume in regions of elevated relative pressure is characteristic of pores formed between the particle agglomerates (macroporosity).

The HA-Eu(2%)-Gd(1%) presented type-H3 hysteresis loop which is often observed with aggregates of plate-like particles that give rise to slit-shape pores [32].The MSN/HA-Eu(2%)-Gd(1%)

and MSN/HA-Eu(2%)-Gd(1%)/P(MAA) samples exhibited H4 hysteresis loops, typical for mesoporous structures with constant cross-section porosity (cylindrical or hexagonal) and three-dimensionally ordered pores with lower or no blockage [19,49].

Furthermore, it is possible to observe that MSN/ HA/Eu(2%)-Gd(1%)/P(MAA) sample exhibited significant reductions in the adsorbed N_2 volume at all relative pressures; this result indicates that the polymerization processes led to significant changes in the pore structure, indicating the presence of polymeric phase in the system, as evidenced by the previous characterization results.

The calculated texture and porosity parameters are presented in Table 4. It is possible to observe a significant increase in surface area after the addition of silica to the system, which can be attributed to the intrinsic characteristics of this material, such as high surface area and pore volume. This feature is essential for nanosystems with an emphasis on drug delivery applications. The surface area obtained for the nanocomposite MSN/HA-Eu(2%)-Gd(1%) of 289.13 $m^2.g^{-1}$ is in agreement with a similar nanocomposite described in the literature, with application in drug delivery [19,22,50].

Table 4. Textural and porosity parameters obtained through BET and BJH methods applied on the N2 adsorption-desorption isotherms data.

Sample	S_{BET} ($m^2.g^{-1}$)	Vp ($cc^3.g^{-1}$)	Dp (nm)
HA-Eu(2%)-Gd(1%)	43	0.106	3.7
MSN/HA-Eu(2%)-Gd(1%)	289	0.167	3.1
MSN/HA-Eu(2%)-Gd(1%)/P(MAA)	120	0.060	3.1

It is observed that after polymerization with P(MAA), there was a reduction in the surface area and the pore volume of the MSN/HA-Eu(2%)-Gd(1%)/P(MAA). This can be ascribed to the hydrogel polymerization occurring both on the surface and inside the pore structure of the MSN/HA-Eu(2%)-Gd(1%) phase [19,51]. The pore size diameters remained unchanged after the hydrogel polymerization, since the BJH method calculates the average value of the nanoparticle diameter without distinguishing the amount of large or small pores present in the sample [19,37].

3.7. Photoluminescence Analysis

The room temperature PL spectra of the samples were measured in a wide wavelength range (300–850 nm) by employing an excitation laser line at $\lambda_{exc} = 457\,nm$, where no emissions were observed between 457 and 600 nm for all samples. Furthermore, as expected, the HA sample does not display significant luminescence in its whole spectrum. Thus, to present more detailed spectra, they were separated into the following two regions: (i) high-energy emissions (300-470 nm) with a total integrated PL intensity named I_1, and (ii) low-energy emissions (550-870 nm) with a total integrated PL intensity named I_2.

Figure 10 presents the PL spectra of all samples measured in the high-energy region (300-470 nm), where, except for the HA sample, the several observed peak emissions could be ascribed according to the indicated radiative transitions between the energy levels of Eu^{3+} ions. No emissions from the levels of the Gd^{3+} ions were identified. Since the laser line (λ_{exc}= 457 nm) has no enough energy to excite the high energy levels of the Eu^{3+} ions, the PL emissions involving these states can only be explained by a complex phonon assisted and cooperative upconversion mechanism of nonradiative energy transfer involving dipole-dipole and dipole-quadrupole interactions between rare earth ions in the nearest neighbor positions, which can be enhanced by exchange coupling between these ions [52–55].

Preprints (www.preprints.org) | NOT PEER-REVIEWED | Posted: 19 May 2023 doi:10.20944/preprints202305.1385.v1

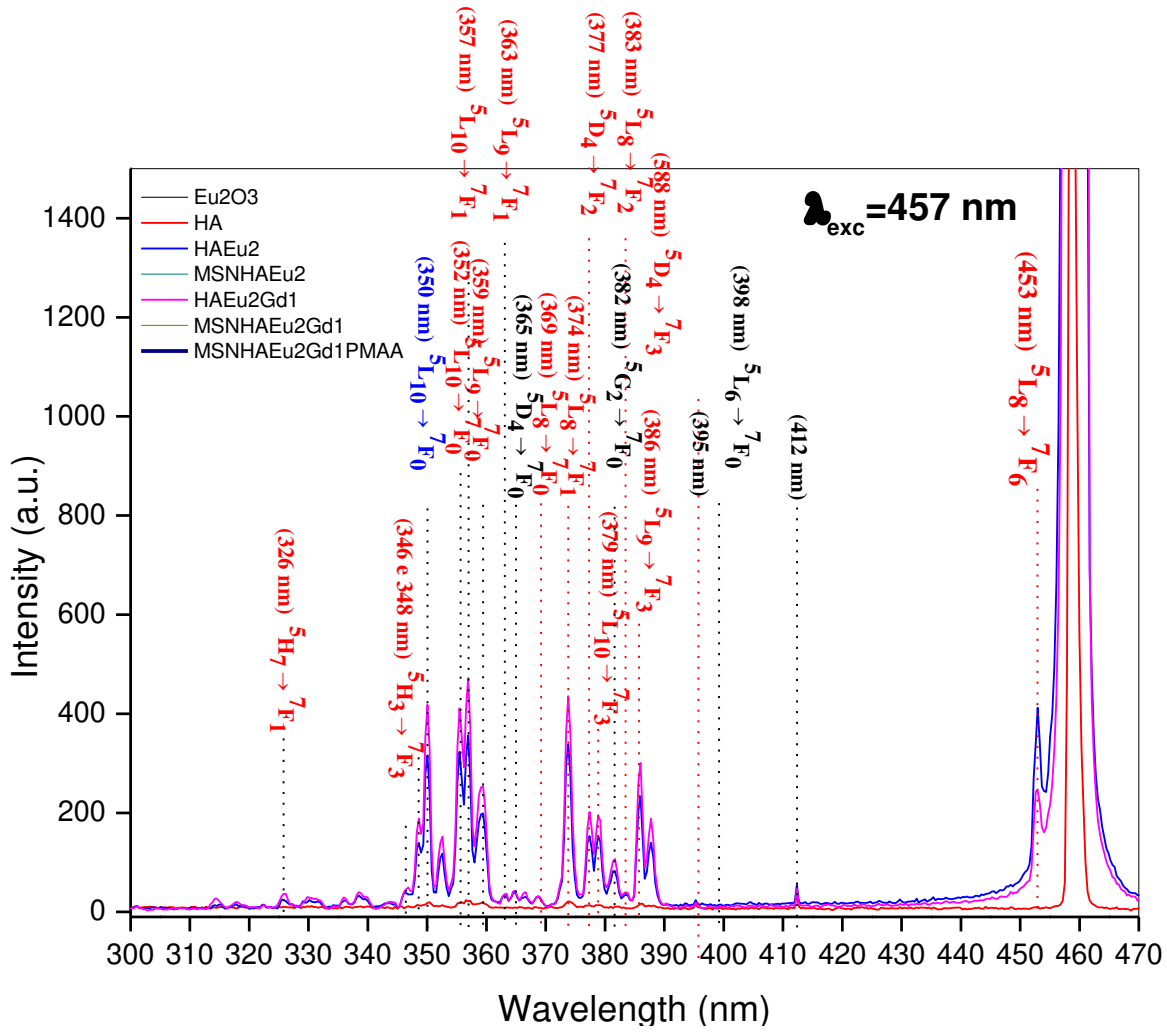

Figure 10. PL spectra of all samples measured in the high-energy region (300-470 nm).

Specifically for the samples with two unlike trivalent rare earth ions, Eu^{3+} and Gd^{3+}, (HA-Eu(2%)-Gd(1%), MSN/HA-Eu(2%)-Gd(1%) and MSN/HA-Eu(2%)-Gd(1%)/P(MAA) samples), this energy transfer mechanism can predominantly be governed by the dipole-quadrupole interaction [53], mainly for the states of the larger rare earth ions that lie high in energy [52].

Figure 11 presents the PL spectra of all samples measured in the low-energy region (550-850 nm), showing several peak emissions excluding the spectrum of the HA sample. As specified in this figure, these emissions were attributed according to the radiative transitions involving the levels of the Eu^{3+} ions: $^5D_1 \rightarrow {}^7F_J$ (J = 4, 5, 6) and $^5D_0 \rightarrow {}^7F_J$ (J = 2, 3, 4, 5, 6). It is interesting to note that the characteristic emissions $^5D_0 \rightarrow {}^7F_0$ (~570–585 nm) and $^5D_0 \rightarrow {}^7F_1$ (~585–600 nm) of Eu^{3+} ions [56] were not observed. This effect can be attributed to the relatively high wavelength of the excitation laser line ($\lambda_{exc} = 457\ nm$) which is activating the transitions indicated in the Figure 11 and deactivating the transitions $^5D_0 \rightarrow {}^7F_J$ (J = 0, 2).

Preprints (www.preprints.org) | NOT PEER-REVIEWED | Posted: 19 May 2023 doi:10.20944/preprints202305.1385.v1

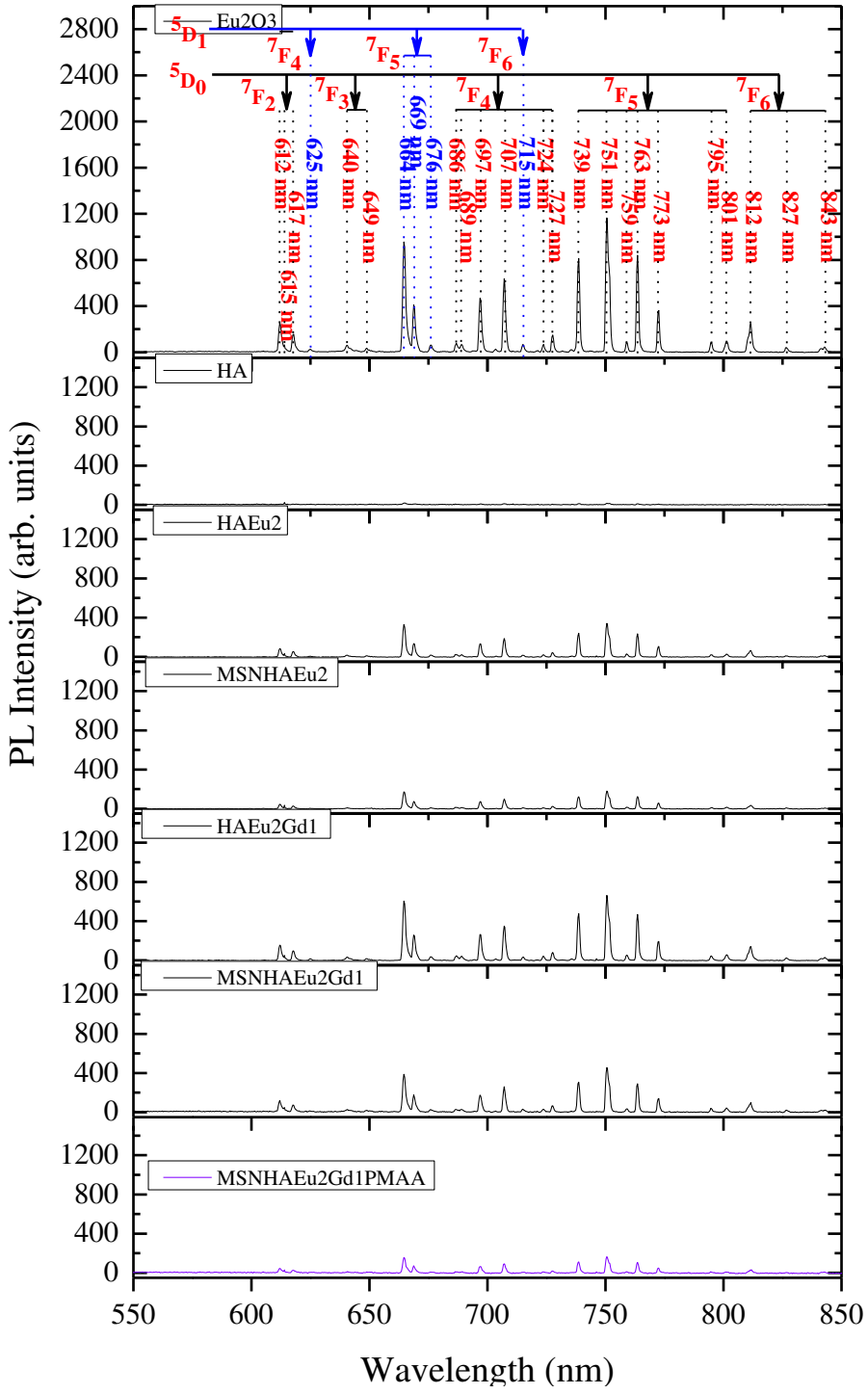

Figure 11. PL spectra of all samples measured in the low-energy region (550-850 nm).

It is also possible to notice in Figure 11 that the addition of gadolinium in the HA-Eu(2%)-Gd(1%) and MSN/HA-Eu(2%)-Gd(1%) samples has caused an enhancement in their PL intensities in comparison to the HA-Eu(2%) and MSN/HA-Eu(2%) samples, respectively. Xie and collaborators obtained a similar result, where the increase in Eu^{3+} luminescence intensity could be observed by co-doping with Gd^{3+}. These authors obtained an increase of 60% to 120% in the emission intensity depending on the molar ratio of the europium and gadolinium content R(Eu/Gd), by explaining this luminescent enhancement phenomenon based on the already mentioned cooperative upconversion mechanism [55] involving the adjacent Eu^{3+} and Gd^{3+} ions.

Preprints (www.preprints.org) | NOT PEER-REVIEWED | Posted: 19 May 2023 doi:10.20944/preprints202305.1385.v1

Figure 12A presents an illustration of this cooperative upconversion mechanism in a Dieke's energy level scheme, where initially the laser line $\lambda_{exc} = 457\ nm\ (\cong 2.71\ eV\ \cong 21{,}881\ cm^{-1})$ can excite by photon absorption, involving phonons due to the nonresonance between the energies, the $^5D_2$ level of the Eu^{3+} ions.

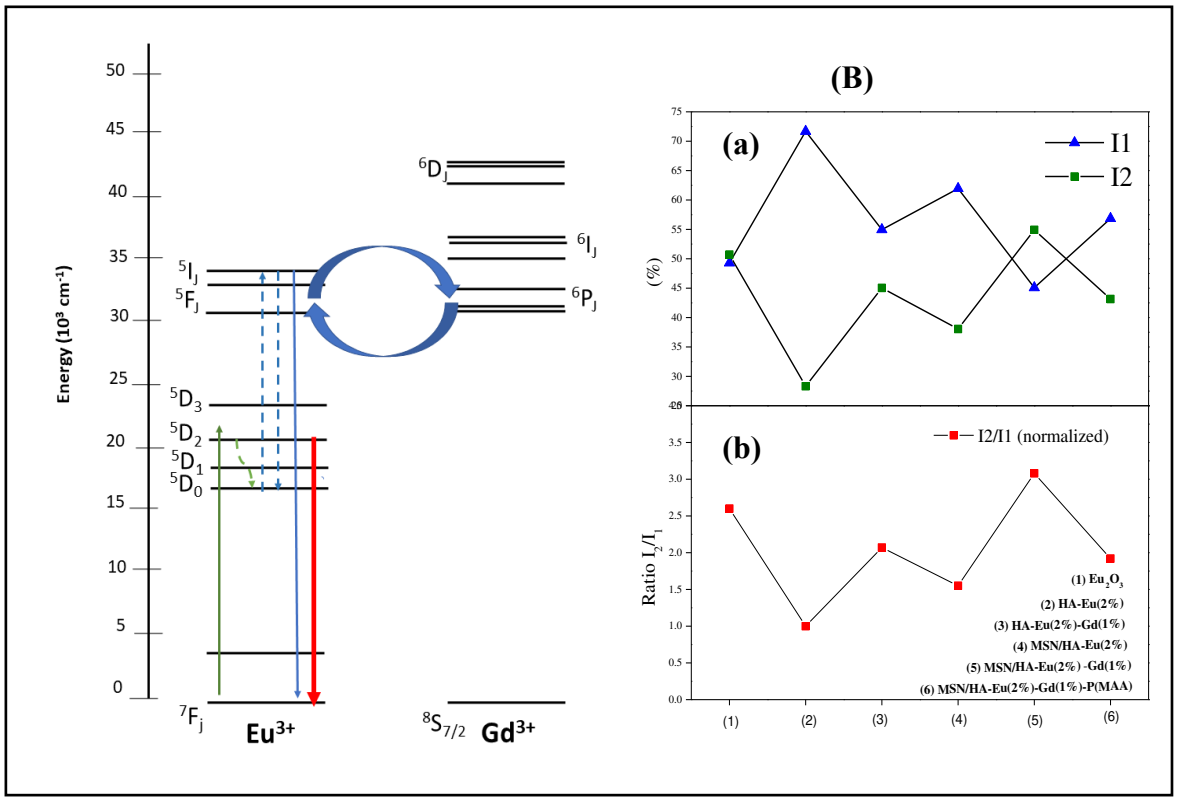

Figure 12. (**A**) Dieke's energy level scheme illustrating the cooperative upconversion mechanism between adjacent trivalent rare earth ions (Eu^{3+} and Gd^{3+}) causing the subsequent enhancement of the enhancement in PL intensities ascribed to the transitions 5D1→7FJ (J = 4, 5, 6) and 5D0→7FJ (J = 2, 3, 4, 5, 6) of Eu3+ ions, and (**B**) Comparison of the percentage total integrated PL intensities, E_1 and E_2 (**a**), and comparison of the ratio I_2/I_1, normalized for HA-Eu(2%) sample (**b**).

Then, a nonradiative thermalization assisted by phonons occurs from the $^5D_2$ to both the $^5D_1$ and $^5D_0$ levels of Eu^{3+} ions, as indicated by the doted wave lines. In sequency, the cooperative upconversion mechanism of nonradiative energy transfer involving dipole-dipole and dipole-quadrupole interactions of the adjacent rare earth ions (Eu^{3+} and Gd^{3+}) takes place promoting excitation of the upper energy levels of the Eu^{3+} ions with consequent nonradiative energy transfer to the ^5P_J levels of the Gd^{3+} ions. Since no emissions from the gadolinium's levels were identified in the high-energy region (300-470 nm) of PL spectra of samples (Figure 10), it is concluded that a back nonradiative energy transfer occurs from the Gd^{3+} to the Eu^{3+} ions. The nonradiative excitation of the upper levels of Gd^{3+} ions and the subsequent back energy transfer to the upper levels of the Eu^{3+} ions are indicated in the Figure 12A by the curved arrows. From the upper energy levels of the Eu^{3+} ions, several radiative emissions were identified in the PL spectra shown in the Figure 10. Finally, a part of energy from the upper energy levels of the Eu^{3+} ions is also returned by nonradiative transitions to their lower energy levels ($^5D_2$, $^5D_1$ and $^5D_0$), causing the enhancement in PL intensities observed in Figure 11 ascribed to the transitions $^5D_1 \rightarrow {}^7F_J$ (J = 4, 5, 6) and $^5D_0 \rightarrow {}^7F_J$ (J = 2, 3, 4, 5, 6).

To quantify this complex cooperative upconversion mechanism of nonradiative energy transfer in the all samples with rare earth ions (Eu^{3+} and Gd^{3+}), it was carried out an analysis of the total integrated PL intensities I_1 and I_2 for the two regions: (i) I_1: high-energy emissions (300-470 nm) (Figure 10), and (ii) I_2: low-energy emissions (550-870 nm) (Figure 11).

Figure 12B(a) shows a comparison of the percentage of these total integrated PL intensities, E_1 and E_2, for these samples with the following values: (i) Eu_2O_3: I_1= 49.29% and I_2=50.71%; (ii) HA-

 doi:10.20944/preprints202305.1385.v1

Eu(2%): I_1= 71.68% and I_2=28.32%; (iii) HA-Eu(2%)-Gd(1%): I_1= 54.96% and I_2=45.04%; (iv) MSN/HA-Eu(2%): I_1= 61.95% and I_2=38.05%; (v) MSN/HA-Eu(2%)-Gd(1%): I_1= 45.09% and I_2=54.91%; (vi) MSN/HA-Eu(2%)-Gd(1%)/P(MAA): I_1= 56.85% and I_2=43.15%. In Figure 14a the HA-Eu(2%) presents a substantial increase of I_1 and decrease of I_2 in comparison with the Eu_2O_3, evidencing the strong cooperative upconversion mechanism between the Eu^{3+} ions in the nearest neighbor positions. The substantial increase of I_1 and decrease of I_2 the HA-Eu(2%) evidences its strong cooperative upconversion mechanism in comparison with the Eu_2O_3 but with a less efficient return of energy, by nonradiative transitions, from the upper energy levels to the lower energy levels of the Eu^{3+} ions. In contrast with the HA-Eu(2%), the growth of I_2 and reduction of I_1 for the HA-Eu(2%)-Gd(1%) confirms that the inclusion of the Gd^{3+} ions has favored the nonradiative back energy transfer to the lower energy levels of the Eu^{3+} ions by enhancing their PL intensities in low-energy emissions (Figure 11). In comparison with the HA-Eu(2%), the MSN/HA-Eu(2%) samples shows increase of I_2 and decrease of I_1, evidencing its better efficiency nonradiative back energy transfer to the lower energy levels of the Eu^{3+} ions. The MSN/HA-Eu(2%)-Gd(1%) sample, in contrast with the MSN/HA-Eu(2%), displays a strong increase of I_2 and decrease of I_1, again evidencing the improvement of the cooperative upconversion mechanism caused the presence of the Gd^{3+} ions with consequent intensification of the PL intensities in low-energy emissions. Finally, in comparison with the MSN/HA-Eu(2%)-Gd(1%), the MSN/HA-Eu(2%)-Gd(1%)/P(MAA) samples has decrease of I_2 and increase of I_1, which can be attributed the functionalization of the nanocomposite with the P(MAA).

In agreement with the results of the Figure 12B(a), the Figure 12B(b) presents a comparison of the ratio I_2/I_1, normalized for HA-Eu(2%) sample, in order to provide a undoubted understanding about the enhancement of the PL intensities in low-energy emissions (550-870 nm) caused by the gadolinium. The HA-Eu(2%)-Gd(1%) and MSN/HA-Eu(2%)-Gd(1%) shows strong growth of the ratio I_2/I_1 , from 1.00 to 2.07 and from 1.55 to 3.08, in comparison with HA-Eu(2%) and MSN/HA-Eu(2%), respectively. Once more, this result confirms the high efficiency cooperative upconversion mechanism of nonradiative energy transfer involving multipolar interactions between Gd^{3+} and Gd^{3+} ions, with the subsequent partial nonradiative back energy transfer from the upper energy levels of the Eu^{3+} ions to their lower energy levels ($^5D_2$, $^5D_1$ and $^5D_0$). Furthermore, the functionalization of the nanocomposite with the P(MAA) in the MSN/HA-Eu(2%)-Gd(1%)/P(MAA) sample has caused the weakening of the cooperative upconversion mechanism, reducing the ratio I2/I1 from 3.08 to 1.92 compared to the MSN/HA-Eu(2%)-Gd(1%), which can be attributed to an energy loss involving the vibrational states of the P(MAA). Nonetheless, this value 1.92 is still very higher (almost double) of the value 1.00 observed for the HA-Eu(2%) sample, evidencing that the nonradiative multipolar energy transfer between Eu3+ and Gd3+ ions is maintained very efficient.

3.8. Vibrant Sample Magnetometry (VSM)

The magnetization properties using vibration sample magnetometer (VSM) of the samples HA, HA-Eu(2%)-Gd(1%) and MSN/HA-Eu(2%)-Gd(1%) were evaluated and are shown in Figure 13. The analysis was measurements were carried out at room temperature. Among the rare earth elements, gadolinium Gd^{3+} possess high magnetic moment due to isotropic electronic ground state $^8S_{7/2}$ and half-filled *f*-orbital with seven electrons. This leads to large effects on both longitudinal and transverse proton relaxivities of Gd^{3+} even at low applied magnetic fields [57].

Preprints (www.preprints.org) | NOT PEER-REVIEWED | Posted: 19 May 2023 doi:10.20944/preprints202305.1385.v1

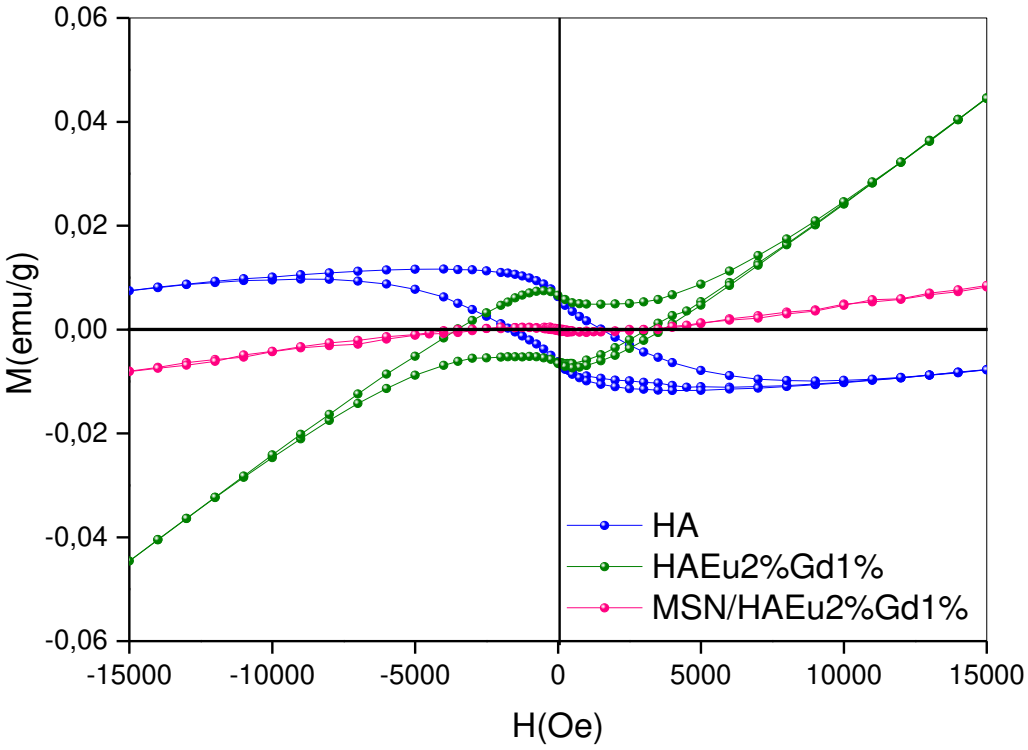

Figure 13. Magnetic properties obtained by magnetometry of vibrating sample, of undoped and Gd-doped HA, HA-Eu(2%)-Gd(1%) and MSN/HA-Eu(2%)-Gd(1%)samples.

The hysteresis loops of the samples, reveal that the presence of gadolinium alters the magnetic behavior of materials [58]. It is possible to observe the diamagnetic signal (DM) of the pure HA sample, while the samples with Gd doping, HA-Eu(2%)-Gd(1%) and MSN/HA-Eu(2%)-Gd(1%), showed a paramagnetic signal (PM). These results were also found in similar works [57,58]. For the MSN/HA-Eu(2%)-Gd(1%) sample, the magnetization level Gd^{3+} decreased with the addition of silica in the system. Considering the results obtained it is reasonable to assume that gadolinium-doped materials have potential applications as contrast agents for MRI, besides being used simultaneously as therapy functions [58].

3.9. Drug Loading and Releasing Results

In this study, we evaluated the incorporation and release of the antitumor drug doxorubicin in the luminescent materials MSN/HA-Eu(2%)-Gd(1%) and MSN/HA-Eu(2%)-Gd(1%)/P (MAA), using UV-VIS spectroscopy. The incorporation efficiency of the antitumor drug doxorubicin in these materials was esti mated. The results obtained were 71% for the MSN/HA-Eu(2%)-Gd(1%) sample and 95% for the MSN/HA-Eu(2%)-Gd(1%) / P(MAA)). It is possible to notice a higher incorporation efficiency (E.I.) of the luminescent hybrid when compared to the MSN/HA-Eu(2%)-Gd(1%) sample. This behavior may be related to the cationic character presented by the doxorubicin molecule (pKa 8.6) which is different from the anionic character presented by the carboxylic group present in methacrylic acid (pKa 5.5-6.0). In this sense, in incorporation conditions with pH around 7.0, these characteristics favor the electrostatic interaction between DOX and the MAA hydrogel, leading to a greater efficiency of drug incorporation [59].

Drug release assays were performed as a function of time for 168 h at two different pH's, 5 and 7 (Figure 14). This test is essential to evaluate the potential of this material for application in controlled drug release, based on the difference in pH that exists between normal and tumor cells. The MSN/HA-Eu(2%)-Gd(1%) sample showed a total release percentage of 22% at pH 5 and 16% at pH 7, indicating that the difference in the medium does not affect significatively the release profile. In the other hand, for the luminescent hybrid system MSN/HA-Eu(2%)- Gd(1%)/P(MAA), it is possible to notice significant changes in the total DOX release values, 27% at pH 5 and 1.5% at pH 7. These results

Preprints (www.preprints.org) | NOT PEER-REVIEWED | Posted: 19 May 2023 doi:10.20944/preprints202305.1385.v1

indicate that the release of DOX from MSN/HA-Eu(2%)-Gd(1%) and MSN/HA-Eu(2%)-Gd(1%)/P(MAA) materials is pH dependent. of the medium, being favored at pH 5. Despite this, a greater responsiveness to the pH of the hybrid system is evident, as expected.

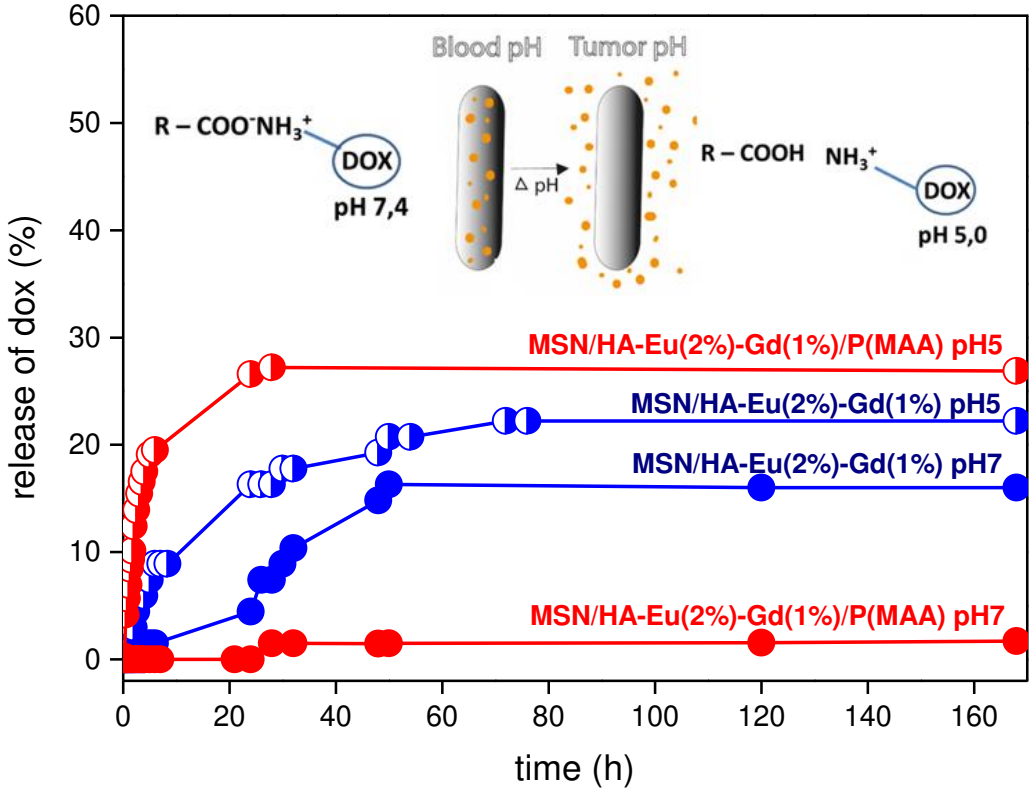

Figure 14. Doxorubicin delivery from a MSN/HA-Eu(2%)-Gd(1%) and MSN/HA-Eu(2%)-Gd(1%)/P(MAA).sample at different pH's.

Possibly, the greater amount of DOX released in the tests performed at pH 5 occurs due to the protonation of the carboxyl groups present in the hydrogel, which results in lower electrostatic interactions between it and the drug. At pH 7, smaller amounts of the drug were released and could probably be related to the strong electrostatic interaction between the DOX molecules and the MAA segments present in the hybrid materials [60]. On the other hand, it is observed that not all incorporated material was released for the two studied samples. Possibly there may be the intermolecular interactions between the materials and the drug occurs through.

The study of dynamic swelling and ionic gel equilibrium in fluids used in controlled drug delivery studies are important to understand the diffusion process [61]. To perform the kinetic studies, the data obtained were adjusted to the Korsmeyer-Peppas equation, represented by the following expression [62–64].

$$\frac{Mt}{Mo} = kt^n$$

where Mt corresponds to drug release at time t, Mo represents the amount of drug initially incorporated into the material, and n is the release index, indicative of the mechanism of drug release, and k is a kinetic constant characteristic of the drug-carrier system.

Peppas (1985) used the value of n to characterize the different release mechanisms, having reached values of n = 0.5 for Fickian diffusion and values of n between 0.5 and 1.0, for mass transfer according to a non-Fickian model. This model is generally used to analyze the release of polymeric dosage forms, when the release mechanism is not well known or when more than one type of release may be involved [65]. Table 5 presents the results of the release kinetics of the drug doxorubicin obtained for the samples MSN/HA-Eu(2%)-Gd(1%) and MSN/HA-Eu(2%)-Gd(1%)/ P (MAA), as well as the correlation coefficients (R^2), used to assess the accuracy of the fit.

Preprints (www.preprints.org) | NOT PEER-REVIEWED | Posted: 19 May 2023 doi:10.20944/preprints202305.1385.v1

Table 5. Kinetic parameters calculated using the Ritger & Peppas model from data on the amount of mass released in the tests performed.

	Samples	Region	n	k	R^2	release mechanism
pH5	MSN/HA-Eu(2%)-Gd(1%)/DOX	(I)	2.41	2.96	1	Super-Case II
		(II)	1.71	0.91	0.996	Super-Case II
		(III)	0.46	3.50	0.984	Fickian diffusion
	MSN/HA-Eu(2%) Gd(1%)/P(MAA)/DOX	(I)	0.72	6.93	0.995	non-fickian diffusion
		(II)	0.47	9.02	0.991	Fickian diffusion
		(III)	0.22	13.2	0.999	Fickian diffusion
pH 7	MSN/HA-Eu(2%)-Gd(1%)/DOX	(I)	0.79	0.36	1	non-fickian diffusion
		(II)	0.96	0.37	0.972	non-fickian diffusion
	MSN/HA-Eu(2%) Gd(1%)/P(MAA)/DOX	(I)	0.04	1.24	1	Fickian diffusion
		(II)	0.28	0.41	1	Fickian diffusion

The regressions that originated the release kinetics data are illustrated in Figure 15. Analyzing the presented curves, it is possible to perceive different inclinations for all samples. Therefore, the graphs were separated by regions and the values (R^2) obtained for all samples were greater than 0.97, indicating that the linear correlation coefficient was ideal.

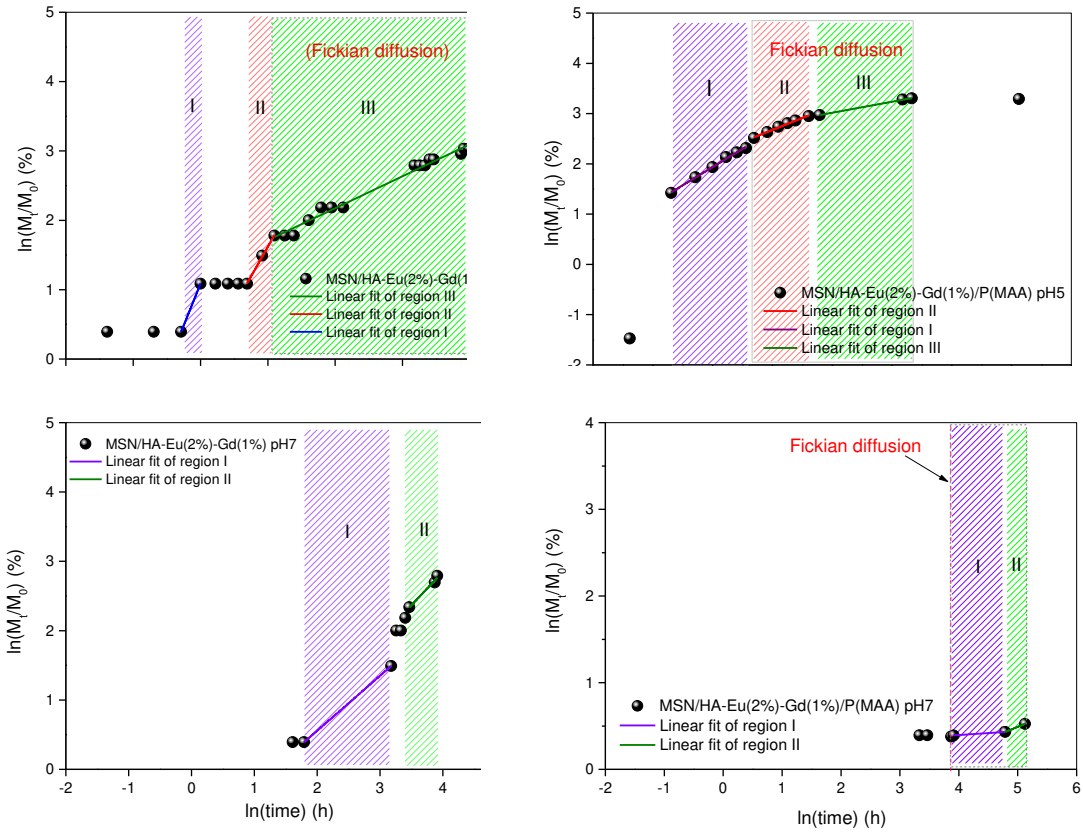

Figure 15. DOX release against time to the power 0.5 for MSN/HA-Eu(2%)-Gd(1%) and MSN/HA-Eu(2%)-Gd(1%)/P(MAA) samples at different pH's.

It can be inferred, for the hybrid system MSN/HA-Eu(2%)-Gd(1%)-P(MAA), that the release model predominantly follows the Fickian diffusion, with $n \leq 0.5$ [66]. Note, for this system, that the test conducted at pH 5 (region I), initially presented a release model that does not follow the Fickian diffusion. This behavior may be related to the burst release, attributed to the desorption of doxorubicin molecules located on the surface of the synthesized materials [32]. Sousa et al. observed that the MCM-41-HA system showed a fast delivery rate during the first 2 hours of the test, releasing about 18% of the incorporated model drug. After that, the system showed a slower rate, with a cumulative release of approximately 45% after 160 h of testing [22].

Furthermore, when analyzing the drug release kinetics for the MSN/HA-Eu(2%)-Gd(1%) nanocomposite, it is observed that for most of the test time, this system does not follow Fickian diffusion. This result demonstrates a more uncontrolled release of the system that does not contain the polymeric phase and reinforces the previously discussed theory that the hybrid system presents a more controlled release of the drug. In addition, it is noted that the MSN/HA-Eu(2%)-Gd(1%)/P(MAA) hybrid system has a higher rate of doxorubicin drug release than MSN/HA-Eu(2%) - Gd(1 %) in pH 5, associated to the visibly greater kinetic constant K, that is related with the drug release rate. In other words, this result shows that the presence of the polymer in the system affects the release kinetics. The influence of the pH of the medium on the release kinetics is also observed, corroborating what was previously discussed.

This result is in line with what was expected in this work, whose objective was to develop a system capable of delivering antitumor drugs at a more acidic pH (tumor region), and not reaching healthy cells, which have a more alkaline pH. This fact demonstrates that the system developed in this work is promising for targeted delivery of antitumoral drug in a targeted and controlled manner from responsive polymers.

The greater control of drug release by the MSN/HA-Eu(2%)-Gd(1%)/P(MAA) luminescent hybrid system, when subjected to pH changes, may indicate that the material developed in this work has the potential to targeted and controlled drug delivery. This release behavior is desirable for cancer treatment, as most of the drug remains encapsulated in the nanocarrier during circulation and when it reaches the acidic tumor tissue, the low pH triggers drug release.

4.Conclusions

In this study, it was demonstrated that a hybrid system composed of silica/hydroxyapatite containing europium and gadolinium was synthesized and the polymerization process with P(MAA), a pH sensitive polymer, was effective. The adequate combination of different characterization techniques allowed us to show the main characteristics of the studied samples. The evidence of the formation of an organic phase of the material was confirmed by the CHN and FTIR techniques. The synthesis of the MSN/HA-Eu(2%)-Gd(1%) nanocomposite was also satisfactory since the results obtained by XRD, FTIR, SEM and TEM characterized the obtained material. The photoluminescence results demonstrated the luminescent potential of europium-doped systems. Furthermore, an improvement in the luminescence of nanoparticles co-doped with europium and gadolinium was observed, which can be explained by the transfer of energy from Gd^{3+} to Eu^{3+}. The potential of the synthesized materials for pH-responsive controlled drug release applications was also confirmed by the doxorubicin drug incorporation and release assay. This test demonstrated that the synthesized system presents a controlled release at pH 5, not releasing significantly at pH 7. This result is satisfactory for drug delivery systems with emphasis on cancer treatment. In addition, promising results for diagnostic imaging applications were observed using photoluminescence and VSM techniques. These techniques confirmed the presence of the rare earth elements europium and gadolinium and demonstrated that the synthesized materials have luminescent and magnetic properties.

Author Contributions: *Rafaela Apostolos*: Conceptualization, Methodology, Investigation, Writing – original draft, Writing – review & editing. *Andreza Sousa Andrada*: Formal analysis, Validation, Writing. *Ernesto Soares de Freitas Neto*: Formal analysis, Investigation, Writing. *André Felipe Oliveira*: Formal analysis, Validation, Writing.

Edésia Sousa: Conceptualization, Investigation, Writing – review & editing, Project administration, Funding acquisition. All authors have read and agreed to the published version of the manuscript.

Funding: This research was supported by the Fundação de Amparo à Pesquisa do Estado de Minas Gerais - FAPEMIG, Conselho Nacional de Desenvolvimento Científico e Tecnológico - CNPq and Coordenação de Aperfeiçoamento de Pessoal de Nível Superior - CAPES.

Data availability: Data will be made available on request.

Acknowledgments: The authors thank the Microscopy Center of the Federal University of Minas Gerais, Belo Horizonte, Brazil for the TEM analyses, and the Fundação de Amparo à Pesquisa do Estado de Minas Gerais— FAPEMIG, Conselho Nacional de Desenvolvimento Científico e Tecnológico— CNPq and Coordenação de Aperfeiçoamento de Pessoal de Nível Superior—CAPES by finalcial support.

References

1. Sarbaz, M.; Manouchehri Monazah, F.; Eslami, S.; Kimiafar, K.; Mousavi Baigi, S.F. Effect of Mobile Health Interventions for Side Effects Management in Patients Undergoing Chemotherapy: A Systematic Review. *Heal. Policy Technol.* **2022**, *11*, 100680, doi:10.1016/j.hlpt.2022.100680.
2. Vyas, M.; Simbo, D.A.; Mursalin, M.; Mishra, V.; Bashary, R.; Khatik, G.L. Drug Delivery Approaches for Doxorubicin in the Management of Cancers. *Curr. Cancer Ther. Rev.* **2019**, *16*, 320–331, doi:10.2174/1573394716666191216114950.
3. Chatterjee, S.; Ghosal, K.; Kumar, M.; Mahmood, S.; Thomas, S. A Detailed Discussion on Interpenetrating Polymer Network (IPN) Based Drug Delivery System for the Advancement of Health Care System. *J. Drug Deliv. Sci. Technol.* **2023**, *79*, 104095, doi:10.1016/j.jddst.2022.104095.
4. Ibrahim-hashim, A.; Estrella, V. Acidosis and Cancer : From Mechanism to Neutralization. **2019**, 149–155.
5. Bhattacharya, S.; Prajapati, B.G.; Singh, S. Jo u Rn a l P. *Crit. Rev. Oncol. / Hematol.* **2023**, 103961, doi:10.1016/j.critrevonc.2023.103961.
6. Ahmadi, M.; Madrakian, T.; Ghoorchian, A.; Kamalabadi, M.; Afkhami, A. *Stimuli-Sensitive Drug Delivery Systems*; Elsevier Ltd., 2020; ISBN 9780081029855.
7. Saadat, M.; Mostafaei, F.; Mahdinloo, S.; Abdi, M.; Zahednezhad, F.; Zakeri-Milani, P.; Valizadeh, H. Drug Delivery of PH-Sensitive Nanoparticles into the Liver Cancer Cells. *J. Drug Deliv. Sci. Technol.* **2021**, *63*, 102557, doi:10.1016/j.jddst.2021.102557.
8. Khan, S.; Vahdani, Y.; Hussain, A.; Haghighat, S.; Heidari, F.; Nouri, M.; Haj Bloukh, S.; Edis, Z.; Mahdi Nejadi Babadaei, M.; Ale-Ebrahim, M.; et al. Polymeric Micelles Functionalized with Cell Penetrating Peptides as Potential PH-Sensitive Platforms in Drug Delivery for Cancer Therapy: A Review. *Arab. J. Chem.* **2021**, *14*, 103264, doi:10.1016/j.arabjc.2021.103264.
9. Xie, A.J.; Yin, H.S.; Liu, H.M.; Zhu, C.Y.; Yang, Y.J. Chinese Quince Seed Gum and Poly (N,N-Diethylacryl Amide-Co-Methacrylic Acid) Based PH-Sensitive Hydrogel for Use in Drug Delivery. *Carbohydr. Polym.* **2018**, *185*, 96–104, doi:10.1016/j.carbpol.2018.01.007.
10. Silva, W.M. da; Monteiro, G.A.A.; Gastelois, P.L.; Sousa, R.G. de; Macedo, W.A. de A.; Sousa, E.M.B. Efficient Sensitive Polymer-Grafted Boron Nitride Nanotubes by Microwave-Assisted Process. *Nano-Structures and Nano-Objects* **2018**, *15*, 186–196, doi:10.1016/j.nanoso.2017.09.014.
11. Baptista, L.; Freitas, D.O.; Melo, L. De; Sousa, B. De Multifunctional Mesoporous Silica Nanoparticles for Cancer-Targeted, Controlled Drug Delivery and Imaging. *Microporous Mesoporous Mater.* **2017**, *242*, 271–283, doi:10.1016/j.micromeso.2017.01.036.
12. Guha, A.; Biswas, N.; Bhattacharjee, K.; Sahoo, N.; Kuotsu, K. PH Responsive Cylindrical MSN for Oral Delivery of Insulin-Design, Fabrication and Evaluation. *Drug Deliv.* **2016**, *23*, 3552–3561, doi:10.1080/10717544.2016.1209796.
13. Rawat, P.; Ahmad, I.; Thomas, S.C.; Pandey, S.; Vohora, D.; Gupta, S.; Ahmad, F.J.; Talegaonkar, S. Revisiting Bone Targeting Potential of Novel Hydroxyapatite Based Surface Modified PLGA Nanoparticles of Risedronate: Pharmacokinetic and Biochemical Assessment. *Int. J. Pharm.* **2016**, *506*, 253–261, doi:10.1016/j.ijpharm.2016.04.049.
14. Sistanipour, E.; Meshkini, A.; Oveisi, H. Catechin-Conjugated Mesoporous Hydroxyapatite Nanoparticle: A Novel Nano-Antioxidant with Enhanced Osteogenic Property. *Colloids Surfaces B Biointerfaces* **2018**, *169*, 329–339, doi:10.1016/j.colsurfb.2018.05.046.
15. Lin, L.; Chow, K.L.; Leng, Y. Study of Hydroxyapatite Osteoinductivity with an Osteogenic Differentiation of Mesenchymal Stem Cells. *J. Biomed. Mater. Res. Part A* **2009**, *89A*, 326–335, doi:10.1002/jbm.a.31994.
16. Ge, J.; Zhang, Q.; Zeng, J.; Gu, Z.; Gao, M. Radiolabeling Nanomaterials for Multimodality Imaging: New Insights into Nuclear Medicine and Cancer Diagnosis. *Biomaterials* **2020**, *228*, doi:10.1016/j.biomaterials.2019.119553.
17. Zhang, M.; Yilmaz, T.; Boztas, A.O.; Karakuzu, O.; Bang, W.Y.; Yegin, Y.; Luo, Z.; Lenox, M.; Cisneros-Zevallos, L.; Akbulut, M. A Multifunctional Nanoparticulate Theranostic System with Simultaneous

Chemotherapeutic, Photothermal Therapeutic, and MRI Contrast Capabilities. *RSC Adv.* **2016**, *6*, 27798–27806, doi:10.1039/c5ra27792b.
18. Yu, Z.; Eich, C.; Cruz, L.J. Recent Advances in Rare-Earth-Doped Nanoparticles for NIR-II Imaging and Cancer Theranostics. *Front. Chem.* **2020**, *8*, 1–10, doi:10.3389/fchem.2020.00496.
19. dos Apostolos, R.C.R.; Cipreste, M.F.; de Sousa, R.G.; de Sousa, E.M.B. Multifunctional Hybrid Nanosystems Based on Mesoporous Silica and Hydroxyapatite Nanoparticles Applied as Potential Nanocarriers for Theranostic Applications. *J. Nanoparticle Res.* **2020**, *22*, doi:10.1007/s11051-020-05105-0.
20. Xie, Y.; He, W.; Li, F.; Shalika, T.; Perera, H. Luminescence Enhanced Co-Doped Hydroxyapatite Nanocrystals as Imaging Agents In Vitro and In Vivo. **2016**, doi:10.1021/acsami.6b01814.
21. Cipreste, M.F.; Rezende, M.R. de; Hneda, M.L.; Peres, A.M.; Cotta, A.A.C.; Teixeira, V. de C.; Macedo, W.A. de A.; Sousa, E.M.B. de Functionalized-Radiolabeled Hydroxyapatite/Tenorite Nanoparticles as Theranostic Agents for Osteosarcoma. *Ceram. Int.* **2018**, *44*, 17800–17811, doi:10.1016/j.ceramint.2018.06.248.
22. Sousa, A.; Souza, K.C.; Sousa, E.M.B. Mesoporous Silica/Apatite Nanocomposite: Special Synthesis Route to Control Local Drug Delivery. *Acta Biomater.* **2008**, *4*, 671–679, doi:10.1016/j.actbio.2007.11.003.
23. Rietveld, H.M. A Profile Refinement Method for Nuclear and Magnetic Structures. *J. Appl. Crystallogr.* **1969**, *2*, 65–71, doi:10.1107/S0021889869006558.
24. Roisnel, T.; Rodríquez-Carvajal, J. WinPLOTR: A Windows Tool for Powder Diffraction Pattern Analysis. *Mater. Sci. Forum* **2001**, *378*, 118–123, doi:10.4028/www.scientific.net/MSF.378-381.118.
25. Verma, G.; Barick, K.C.; Manoj, N.; Sahu, A.K.; Hassan, P.A. Rod-like Micelle Templated Synthesis of Porous Hydroxyapatite. *Ceram. Int.* **2013**, *39*, 8995–9002, doi:10.1016/j.ceramint.2013.04.100.
26. Marinho, J.P.N.; Gastelois, P.L.; Macedo, W.A. de A.; Cipreste, M.F.; Sousa, E.M.B. Nanostructured System Based on Hydroxyapatite and Curcumin: A Promising Candidate for Osteosarcoma Therapy. *5ht Int. Caparica Symp. nanoparticles/nanomaterials Appl. 2022, 5., 2022, Caparica, Port.* **2023**, doi:10.1016/j.ceramint.2023.03.115.
27. Aldén, K.-I.; Lindqvist, I. X-Ray Studies of Some Apatites. *Zeitschrift für Anorg. und Allg. Chemie* **1964**, *328*, 219–222, doi:10.1002/zaac.19643280503.
28. Brasseur, H. Considerations Nouvelles Sur La Constitution Possible de Phosphate Tricalcique Hydrate. *Cl. Sci.* **1958**, *44*, 507–513.
29. Song, X.; Liu, X.; Ma, Y.; Zhu, Q.; Bi, M. Synthesis of Ce/Gd@HA/PLGA Scaffolds Contributing to Bone Repair and MRI Enhancement. *Front. Bioeng. Biotechnol.* **2022**, *10*, 1–16, doi:10.3389/fbioe.2022.834226.
30. Ignjatović, N.L.; Mančić, L.; Vuković, M.; Stojanović, Z.; Nikolić, M.G.; Škapin, S.; Jovanović, S.; Veselinović, L.; Uskoković, V.; Lazić, S.; et al. Rare-Earth (Gd3+,Yb3+/Tm3+, Eu3+) Co-Doped Hydroxyapatite as Magnetic, up-Conversion and down-Conversion Materials for Multimodal Imaging. *Sci. Rep.* **2019**, *9*, 16305, doi:10.1038/s41598-019-52885-0.
31. Get'man, E.I.; Loboda, S.N.; Tkachenko, T. V.; Yablochkova, N. V.; Chebyshev, K.A. Isomorphous Substitution of Samarium and Gadolinium for Calcium in Hydroxyapatite Structure. *Russ. J. Inorg. Chem.* **2010**, *55*, 333–338, doi:10.1134/S0036023610030058.
32. Vieira, L.A.F.; Meireles, I.B. da C.J.; Sousa, E.M.B. Boron Nitride Nanostructures Reinforced Nanohydroxyapatite: Bifunctional Nanocomposite for Potential Orthopedical Use and Ciprofloxacin Controlled Delivery. *J. Ceram. Process. Res.* **2022**, *23*, 725–736, doi:10.36410/jcpr.2022.23.5.725.
33. Zhao, X.S.; Lu, G.Q.; Whittaker, a K.; Millar, G.J.; Zhu, H.Y. Comprehensive Study of Surface Chemistry of MCM-41 Using Si-29 CP/MAS NMR, FTIR, Pyridine-TPD, and TGA. *J. Phys. Chem. B* **1997**, *101*, 6525–6531, doi:10.1021/jp971366+.
34. Zholobenko, V.L.; Holmes, S.M.; Cundy, C.S.; Dwyer, J. Synthesis of MCM-41 Materials: An in Situ FTIR Study. *Microporous Mater.* **1997**, *11*, 83–86, doi:10.1016/S0927-6513(97)00033-3.
35. Chen, J.; Li, Q.; Xu, R.; Xiao, F. Distinguishing the Silanol Groups in the Mesoporous Molecular Sieve MCM-41. *Angew. Chemie Int. Ed. English* **1996**, *34*, 2694–2696, doi:10.1002/anie.199526941.
36. Shi, J.Y.; Yao, Q.Z.; Li, X.M.; Zhou, G.T.; Fu, S.Q. Controlled Morphogenesis of Amorphous Silica and Its Relevance to Biosilicification. *Am. Mineral.* **2012**, *97*, 1381–1393, doi:10.2138/am.2012.4081.
37. Apostolos, R.C.R.; Andrade, G.F.; Silva, W.M.; Assis Gomes, D.; Miranda, M.C.; Sousa, E.M.B. Hybrid Polymeric Systems of Mesoporous Silica/Hydroxyapatite Nanoparticles Applied as Antitumor Drug Delivery Platform. *Int. J. Appl. Ceram. Technol.* **2019**, *16*, 1836–1849, doi:10.1111/ijac.13231.
38. Sousa, A. de Híbridos de Gel Polimérico Em Sílica Mesoporosa Estruturalmente Ordenada Para Liberação Controlada de Fármacos, Universidade Federal de Minas Gerais, 2009.
39. Baghaei, B.; Jafari, S.H.; Khonakdar, H.A.; Wagenknecht, U.; Heinrich, G. Novel Thermosensitive Hydrogel Composites Based on Poly(D,L -Lactide- Co -Glycolide) Nanoparticles Embedded in Poly(n -Isopropyl Acrylamide) with Sustained Drug-Release Behavior. *J. Appl. Polym. Sci.* **2014**, *131*, n/a-n/a, doi:10.1002/app.40625.
40. Silva, W.M. da; Monteiro, G.A.A.; Gastelois, P.L.; Sousa, R.G. de; Macedo, W.A. de A.; Sousa, E.M.B. Efficient Sensitive Polymer-Grafted Boron Nitride Nanotubes by Microwave-Assisted Process. *Nano-Structures & Nano-Objects* **2018**, *15*, 186–196, doi:10.1016/j.nanoso.2017.09.014.

41. Victor, S.P.; Paul, W.; Jayabalan, M.; Sharma, C.P. Supramolecular Hydroxyapatite Complexes as Theranostic Near-Infrared Luminescent Drug Carriers. *CrystEngComm* **2014**, *16*, 9033–9042, doi:10.1039/c4ce01137f.
42. Bansal, R.; Singh, R.; Kaur, K. Quantitative Analysis of Doxorubicin Hydrochloride and Arterolane Maleate by Mid IR Spectroscopy Using Transmission and Reflectance Modes. *BMC Chem.* **2021**, *15*, 1–11, doi:10.1186/s13065-021-00752-3.
43. Ignjatović, N.L.; Mančić, L.; Vuković, M.; Stojanović, Z.; Nikolić, M.G.; Škapin, S.; Jovanović, S.; Veselinović, L.; Uskoković, V.; Lazić, S.; et al. Rare-Earth (Gd3+,Yb3+/Tm3+, Eu3+) Co-Doped Hydroxyapatite as Magnetic, up-Conversion and down-Conversion Materials for Multimodal Imaging. *Sci. Rep.* **2019**, *9*, 16305, doi:10.1038/s41598-019-52885-0.
44. Narayan, R.; Nayak, U.; Raichur, A.; Garg, S. Mesoporous Silica Nanoparticles: A Comprehensive Review on Synthesis and Recent Advances. *Pharmaceutics* **2018**, *10*, 118, doi:10.3390/pharmaceutics10030118.
45. Ngoune, R.; Peters, A.; von Elverfeldt, D.; Winkler, K.; Pütz, G. Accumulating Nanoparticles by EPR: A Route of No Return. *J. Control. Release* **2016**, *238*, 58–70, doi:10.1016/j.jconrel.2016.07.028.
46. Lopes, M.A.; Monteiro, F.J.; Santos, J.D.; Serro, A.P.; Saramago, B. Hydrophobicity, Surface Tension, and Zeta Potential Measurements of Glass-Reinforced Hydroxyapatite Composites. *J. Biomed. Mater. Res.* **1999**, *45*, 370–375, doi:10.1002/(SICI)1097-4636(19990615)45:4<370::AID-JBM12>3.0.CO;2-0.
47. Suzuki, T.; Nishizawa, K.; Yokogawa, Y.; Nagata, F.; Kawamoto, Y.; Kameyama, T. Time-Dependent Variation of the Surface Structure of Bioceramics in Tissue Culture Medium and the Effect on Adhesiveness of Cells. *J. Ferment. Bioeng.* **1996**, *81*, 226–232, doi:10.1016/0922-338X(96)82213-6.
48. Liberman, A.; Mendez, N.; Trogler, W.C.; Kummel, A.C. Synthesis and Surface Functionalization of Silica Nanoparticles for Nanomedicine. *Surf. Sci. Rep.* **2014**, *69*, 132–158, doi:10.1016/j.surfrep.2014.07.001.
49. Sing, K.S.W. Reporting Physisorption Data for Gas/Solid Systems with Special Reference to the Determination of Surface Area and Porosity (Recommendations 1984). *Pure Appl. Chem.* **1985**, *57*, 603–619, doi:10.1351/pac198557040603.
50. Yousefpour, M.; Taherian, Z. The Effects of Ageing Time on the Microstructure and Properties of Mesoporous Silica-Hydroxyapatite Nanocomposite. *Superlattices Microstruct.* **2013**, *54*, 78–86, doi:10.1016/j.spmi.2012.11.002.
51. Park, M.; Komarneni, S. Stepwise Functionalization of Mesoporous Crystalline Silica Materials. *Microporous Mesoporous Mater.* **1998**, *25*, 75–80, doi:10.1016/S1387-1811(98)00173-5.
52. Van Uitert, L.G. Characterization of Energy Transfer Interactions between Rare Earth Ions. *J. Electrochem. Soc.* **1967**, *114*, 1048, doi:10.1149/1.2424184.
53. Nakazawa, K.; Shionoya, S. Energy Transfer between Trivalent Rare-Earth Ions in Inorganic Solids. *J. Chem. Phys.* **1967**, *47*, 3267–3270, doi:10.1063/1.1712377.
54. Honma, T.; Toda, K.; Ye, Z.G.; Sato, M. Concentration Quenching of the Eu3+-Activated Luminescence in Some Layered Perovskites with Two-Dimensional Arrangement. *J. Phys. Chem. Solids* **1998**, *59*, 1187–1193, doi:10.1016/S0022-3697(98)00056-0.
55. Xie, Y.; He, W.; Li, F.; Perera, T.S.H.; Gan, L.; Han, Y.; Wang, X.; Li, S.; Dai, H. Luminescence Enhanced Eu3+/Gd3+ Co-Doped Hydroxyapatite Nanocrystals as Imaging Agents in Vitro and in Vivo. *ACS Appl. Mater. Interfaces* **2016**, *8*, 10212–10219, doi:10.1021/acsami.6b01814.
56. Binnemans, K. Interpretation of Europium(III) Spectra. *Coord. Chem. Rev.* **2015**, *295*, 1–45, doi:10.1016/j.ccr.2015.02.015.
57. Ashokan, A.; Menon, D.; Nair, S.; Koyakutty, M. A Molecular Receptor Targeted, Hydroxyapatite Nanocrystal Based Multi-Modal Contrast Agent. *Biomaterials* **2010**, *31*, 2606–2616, doi:10.1016/j.biomaterials.2009.11.113.
58. Cipreste, M.F.; Peres, A.M.; Cotta, A.A.C.; Aragón, F.H.; Antunes, A.D.M.; Leal, A.S.; Macedo, W.A.A.; de Sousa, E.M.B. Synthesis and Characterization of 159 Gd-Doped Hydroxyapatite Nanorods for Bioapplications as Theranostic Systems. *Mater. Chem. Phys.* **2016**, *181*, 301–311, doi:10.1016/j.matchemphys.2016.06.063.
59. Salehi, R.; Irani, M.; Eskandani, M.; Nowruzi, K.; Davaran, S.; Haririan, I. Interaction, Controlled Release, and Antitumor Activity of Doxorubicin Hydrochloride From PH-Sensitive P(NIPAAm-MAA-VP) Nanofibrous Scaffolds Prepared by Green Electrospinning. *Int. J. Polym. Mater. Polym. Biomater.* **2014**, *63*, 609–619, doi:10.1080/00914037.2013.854234.
60. Salehi, R.; Rasouli, S.; Hamishehkar, H. Smart Thermo/PH Responsive Magnetic Nanogels for the Simultaneous Delivery of Doxorubicin and Methotrexate. *Int. J. Pharm.* **2015**, *487*, 274–284, doi:10.1016/j.ijpharm.2015.04.051.
61. Khare, A.R.; Peppas, N.A. Swelling/Deswelling of Anionic Copolymer Gels. *Biomaterials* **1995**, *16*, 559–567, doi:10.1016/0142-9612(95)91130-Q.
62. Ritger, P.L.; Peppas, N.A. A Simple Equation for Description of Solute Release I. Fickian and Non-Fickian Release from Non-Swellable Devices in the Form of Slabs, Spheres, Cylinders or Discs. *J. Control. Release* **1987**, *5*, 23–36, doi:10.1016/0168-3659(87)90034-4.

63. Ritger, P.L.; Peppas, N.A. A Simple Equation for Description of Solute Release II. Fickian and Anomalous Release from Swellable Devices. *J. Control. Release* **1987**, *5*, 37–42, doi:10.1016/0168-3659(87)90035-6.
64. Korsmeyer, R.W.; Gurny, R.; Doelker, E.; Buri, P.; Peppas, N.A. Mechanisms of Solute Release from Porous Hydrophilic Polymers. *Int. J. Pharm.* **1983**, *15*, 25–35, doi:10.1016/0378-5173(83)90064-9.
65. Peppas *Pharmaceutical Acta Helvetiae*. 1985, pp. 110–111.
66. Liu, L.; Zeng, J.; Zhao, X.; Tian, K.; Liu, P. Independent Temperature and PH Dual-Responsive PMAA/PNIPAM Microgels as Drug Delivery System: Effect of Swelling Behavior of the Core and Shell Materials in Fabrication Process. *Colloids Surfaces A Physicochem. Eng. Asp.* **2017**, *526*, 48–55, doi:10.1016/j.colsurfa.2016.11.007.